Palatal segment contributions to midfacial anterior-posterior growth

Short running page heading: **Palatal segment contributions to midfacial growth**

Ian C. Welsh @X – 1) Program in Craniofacial Biology, 2) Department of Orofacial Sciences and 3) Department of Anatomy, University of California at San Francisco, San Francisco, California 94143, USA

Maria E. Feiler – Interdepartmental Doctoral Program in Anthropological Sciences, Stony Brook University, Stony Brook, NY 11790

Danika Lipman @Y – Department of Cell Biology and Anatomy, University of Calgary

Isabel Mormile – Interdepartmental Doctoral Program in Anthropological Sciences, Stony Brook University, Stony Brook, NY 11790

Karissa Hansen – 1) Program in Craniofacial Biology, 2) Department of Orofacial Sciences and 3) Department of Anatomy, University of California San Francisco, San Francisco, CA 94143

Christopher J. Percival* – Department of Anthropology, Stony Brook University, Stony Brook NY 11794

* = Corresponding Author: Department of Anthropology, Circle Road, SBS Building S-501, Stony Brook, NY 11994, christopher.percival@stonybrook.edu

@X Present Address: The Jackson Laboratory, 600 Main St. Bar Harbor, ME 04609

@Y Present Address: Department of Mathematics and Statistics, 612 Campus Place NW, University of Calgary, Calgary, AB

Abstract

Anterior-posterior (A-P) elongation of the palate is a critical aspect of integrated midfacial morphogenesis. Reciprocal epithelial-mesenchymal interactions drive secondary palate elongation that is coupled to the periodic formation of signaling centers within the rugae growth zone (RGZ). However, the relationship between RGZ driven morphogenetic processes, the differentiative dynamics of underlying palatal bone mesenchymal precursors, and the segmental organization of the upper jaw has remained enigmatic. A detailed ontogenetic study of these relationships is important, because palatal segment growth is a critical aspect of normal midfacial growth, can be modified to produce dysmorphology, and is a likely basis for evolutionary differences in upper jaw morphology. Variation in palatal-segment specific growth may also underlie known differences in palatal segment proportions between inbred mouse strains. We completed a combined whole mount gene expression and morphometric analysis of normal murine palatal growth dynamics and their association with palatal segment elongation and resulting upper jaw morphology. Our results demonstrated that the first formed palatal ruga (ruga 1), found just posterior to the RGZ, maintained an association with important nasal, neurovascular and palatal structures throughout early midfacial development; suggesting that these features are positioned at a proximal source of embryonic midfacial directional growth. Our detailed characterization of midfacial morphogenesis revealed a one-to-one relationship between palatal segments and upper jaw bones during the earliest stages of palatal elongation. Growth of the maxillary anlage within the anterior secondary palate is uniquely coupled to RGZ-driven morphogenesis that more than doubles the length of this palatal segment prior to palatal shelf fusion. Our results also demonstrate that the future maxillary-palatine suture, approximated by the position ruga 1 and consistently associated with the palatine anlage, forms predominantly

via the posterior differentiation of the maxilla within the expanding anterior secondary palate. Our complementary ontogenetic comparison of three inbred mouse strains identified small but significant strain-specific differences in early embryonic palatal segment contributions to the upper jaw. Although early palatal segment specific growth is not primarily responsible for adult differences in upper jaw morphology between these strains, our ontogenetic series of measurements provide a useful foundation for understanding the impact of background genetic effects on facial shape and elongation. In combination, our results provide a novel and particularly detailed picture of the earliest spatiotemporal dynamics of intramembranous midfacial skeletal specification and differentiation within the context of the surrounding palatal segment A-P elongation and associated rugae formation.

Keywords: palatogenesis, secondary palate, rugae, face elongation, *Mus musculus,* RRID:IMSR_JAX:003715, RRID:IMSR_JAX:001976, RRID:IMSR_JAX:000664

Abbreviations: anterior-posterior (A-P), cranial neural crest (CNC), frontonasal process (FNP), High resolution episcopic microscopy (HREM), maxillary processes (MxP), medial nasal processes (mnp), micro-computed tomography (µCT), rugae growth zone (RGZ), transcription factors (TFs), Whole mount in situ hybridization (WISH)

Introduction

Morphological variation of the midfacial complex, which consists of the nose, upper jaw, cheek, and palate, is a defining aspect of both intra- and inter-specific differences in facial shape. Basic facial shape is the result of cranial neural crest (CNC)-derived facial prominence

outgrowth and fusion, which occur between embryonic day (E) 10 and E15 in mice (Fig. 1). Initial fusion between the medial nasal processes (mnp) of the frontonasal process (FNP) and the anterior maxillary processes (MxP) gives rise to the primary palate and lip, producing a unified upper jaw from previously separated tissues. Secondary palate morphogenesis then begins through outgrowth of the nascent palatal shelf along the medial aspect of the MxP. Significant palatal growth along the anterior-posterior (A-P) axis is accompanied by vertical growth of the palatal shelves prior to their elevation and medial fusion dorsal to the tongue, after which the palatal shelf separates the oral and nasal cavities (Bush and Jiang, 2012; Hammond and Dixon, 2022). Disproportional growth of FNP or MxP prior to fusion can result in cleft lip and palate (Young et al., 2014), while poor coordination between the multiple growth axes of MxP-derived tissues can prevent secondary palate closure even when the palatal shelves maintain competency to fuse (Kouskoura, et al., 2013).

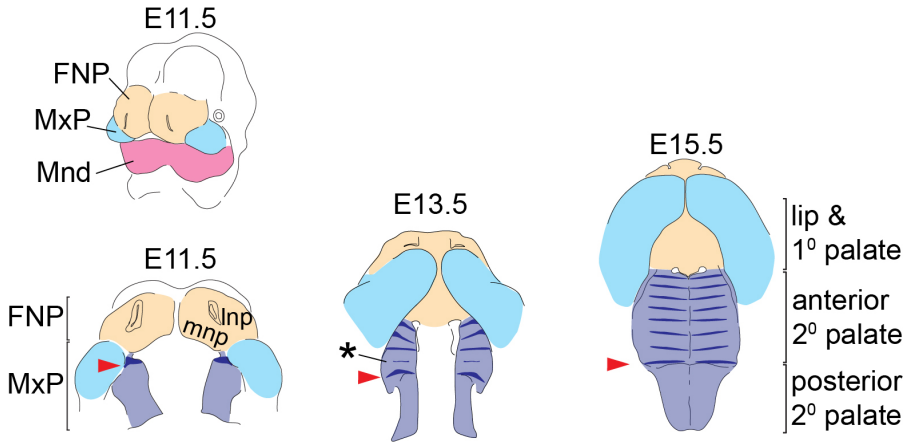

Figure 1 – Tissue origins of the midfacial complex and rugae position during secondary palate morphogenesis – The upper and lower jaws are formed from the frontonasal process (FNP - tan), and branchial arch 1 derived maxillary and mandibular processes (MxP - pale blue and Mnd – magenta, respectively). From E11.5 to E15.5, outgrowth and fusion of the medial nasal process (mnp) with the superficial portion of the MxP frame out the lip and primary (1°) palate, while the A-P elongation and medially directed growth of the palatal shelves from the internal portion of the MxP gives rise to the secondary palate (2° pal – light purple). *Shh* expression (dark blue) highlights the dynamics of rugae formation and illustrates regional expansion of the anterior secondary palate. At E11.5, ruga 1 (red arrowheads) forms at the anterior extent of the nascent palatal shelf and subsequently defines the caudal end of the rugae growth zone (asterisk) where new rugae form prior to being displaced anteriorly. Additional abbreviation: lateral nasal process (lnp).

86

87 Species-specific differences in the size, shape, and growth trajectories of facial
88 prominences are identifiable during the earliest phases of facial morphogenesis, prior to skeletal
89 differentiation, often presaging interspecies differences in adult facial shape (Selleri and Rijli,
90 2023). After initial facial prominence fusion, differential A-P growth of FNP and MxP derived
91 tissues is a major basis for evolutionary differences in midfacial prognathism (Young et al.,
92 2014); possibly based on the balance of CNC progenitor self-renewal versus osteoblast
93 differentiation (Hall et al., 2014; Morris and Abzhanov, 2021; Schneider, 2015). The regional
94 basis for facial elongation varies across taxa; primarily driven by MxP growth in mammals and
95 by FNP growth in birds (Young et al., 2014), indicating different palatal segment contributions.
96 The three longitudinal segments of the palate are called the primary palate, anterior
97 secondary palate, and posterior secondary palate (Fig. 1). The boundary between primary palate
98 and anterior secondary palate is the posterior edge of the fused mnp. Although A-P organization
99 of the secondary palate can be defined by the presence of boney versus muscular tissue (i.e. the
100 hard versus soft palate) or modes of palatal shelf elevation and closure (reviewed by Yu and
101 Ornitz, 2011), we define secondary palate segments by molecular differences in tissue patterning
102 and cell signaling competence (Hilliard et al., 2005; Hammond and Dixon, 2022).
103 The A-P expression domains of certain transcription factors (TFs) and intercellular
104 signaling molecules within CNC-derived mesenchyme are important for A-P organization and
105 growth during palatal morphogenesis. For example, *Msx1* and *Shox2* are exclusively expressed in
106 the anterior secondary palate while *Barx1* and *Tbx22* are exclusive to the posterior secondary
107 palate within this mesenchyme (Hilliard et al., 2005; Okano et al., 2006; Welsh et al., 2018).
108 Mutations of *Shox2* or *Tbx22* have resulted in midline clefts of the anterior or posterior palate,

respectively (Yu et al., 2005; Pauws et al., 2009), although regional expression is maintained in genetically engineered mice with severe segmental growth defects (Welsh et al., 2018). The A-P expression boundary of these and other factors is found at the first formed palatal ruga (Hilliard et al., 2005; Li and Ding, 2007; Welsh et al., 2007; Welsh and O'Brien, 2009; Welsh et al., 2018; Hammond and Dixon, 2022), one of multiple parallel epithelial thickenings on the anterior secondary palate.

This first ruga (ruga 1 numbered according to Welsh et al., 2007, Welsh and O'Brien, 2009; although Pantalacci et al., 2008 use a different numbering system) forms at E11.5 on the anterior extent of the nascent secondary palate (red arrow in Fig. 1). Remaining rugae form sequentially within the rugae growth zone (RGZ) located just anterior to ruga 1 (Welsh and O'Brien, 2009), via a Turing type mechanism (Economou et al., 2012; Kawasaki et al., 2018). Rugae are centers of Sonic Hedgehog signaling (SHH), which is critical for anterior secondary palatal patterning and A-P growth. As the secondary palate completes midline fusion at E15.5, the last formed ruga appears adjacent to ruga 1 in the middle of the secondary palate while each precedingly formed ruga is found at an increasingly anterior position along the anterior secondary palate (Welsh and O'Brien, 2009).

Based upon the dynamics of rugae formation, palate growth, and patterning gene expression, Pantalacci (et al., 2008) hypothesized that ruga 1 represents a distinct morphological boundary related to either the future hard versus soft palate boundary or the maxillary-palatine suture. However, the degree to which rugae formation and regional A-P patterns of secondary palate gene expression are coordinated with palate skeletal differentiation remain unclear. To address this knowledge gap, we mapped markers associated with the specification and differentiation of osteoblasts within the context of secondary palate segmental organization,

132 across a developmental time course spanning mouse secondary palate morphogenesis and upper
133 jaw outgrowth (E11.5-E15.5). Our results indicate that ruga 1 is coincident with the future
134 position of the maxillary-palatine suture, illustrate the one-to-one palatal segment origins of
135 upper jaw bones, and reveal a previously unappreciated coupling of maxillary formation to rugae
136 morphogenesis during elongation of the anterior secondary palate.

137 Given 1) the strong early one-to-one association between forming upper jaw bones and
138 palatal segment specific growth factor expression and 2) that embryonic morphogenesis is
139 critical for the production of typical facial shape (e.g., Hilliard et al., 2005; Kaucka et al., 2018;
140 Yuan et al., 2020), it's possible that early differences in the longitudinal growth of the three
141 palatal segments underlie inter- and intraspecies differences in upper jaw morphology.
142 Specifically, we hypothesized that genetically based differences in palate segment-specific A-P
143 outgrowth would explain previously identified variation in the contribution of the premaxilla,
144 maxilla, and palatine bones to adult upper jaw morphology of inbred mouse strains.

145 C57BL/6J (RRID:IMSR_JAX:000664) inbred strain adults have a relatively long
146 premaxilla, while NOD/ShiLtJ (RRID:IMSR_JAX:001976) have a relatively long maxilla,
147 making them a straightforward comparison. The PWK/PhJ (RRID:IMSR_JAX:003715) wild-
148 derived inbred strain also has a relatively long maxilla, but a proportionally long upper jaw for
149 its small body size (Percival et al., 2016), allowing a test of whether these NOD/ShiLtj-like bone
150 length proportions are the result of similar palatal segment growth trajectories. One possible
151 mechanism for the C57BL/6J strain's relatively short adult maxillary bone might be a slower rate
152 of anterior secondary palate elongation between E11.5 and E15.5. If this type of variation in
153 early A-P elongation of longitudinal palatal shelf segments is the causal basis for strain specific
154 differences in upper jaw morphology, we predicted that C57BL/6J mice would have a relatively

155 long primary palate and a relatively short anterior secondary palate by E15 and that the other two
156 strains would both display relatively long anterior secondary palates at the same developmental
157 stage.

158 Understanding how genetically based differences in early craniofacial development
159 produce morphological variation within model organisms is an important step in determining
160 how these developmental processes can be modified to produce evolutionary differences in upper
161 jaw morphology (Boughner et al., 2008; Hallgrímsson et al., 2009; Fish, 2019; Morris and
162 Abzhanov, 2021), including facial length and the relative contribution of specific bones to the
163 upper jaw. Overall, our multifaceted analysis of ontogenetic trends in palatal and facial
164 elongation provides a novel contextual framework and developmental perspective within which
165 to evaluate the impact of both non-pathogenic and pathogenic genetic differences on midfacial
166 growth and differentiation.

167

168 **Methods**

169 **Specimen and Image Acquisition**

170 Animal breeding, specimen collection, and tissue fixation were performed in accordance
171 with the protocols of the University of California, San Francisco Institutional Animal Care and
172 Use Committee under protocol approval number AN192776-01F. Mice were socially housed
173 under a twelve-hour light-dark cycle with food and water *ad libitum*. Additional enrichment was
174 provided when single housing was required for breeding purposes. Mice were euthanized by CO_2
175 inhalation followed by cervical dislocation or decapitation. Embryos of C57BL/6J
176 (RRID:IMSR_JAX:000664; hereafter referred to as C57), NOD/ShiLtJ
177 (RRID:IMSR_JAX:001976; hereafter referred to as NOD), and PWK/PhJ

178 (RRID:IMSR_JAX:003715; hereafter referred to as PWK) strains (Jackson Labs, Bar Harbor,
179 ME) were collected between gestational days E11.5 and E15.5, as determined from copulatory
180 plug occurrence. Postnatal day one (P1) C57 (n=10) and NOD (n=7) specimens were collected
181 one day after birth. Embryo and P1 specimens were fixed in 4% PFA and stored in 1x PBS for
182 micro-computed tomography (µCT) imaging or dehydrated through a graded PBST-MeOH
183 series and stored at -20°C until use for in situ hybridization. A flowchart provides an overview of
184 our study design (Fig. 2).

185
186
187
188
189
190
191
192
193

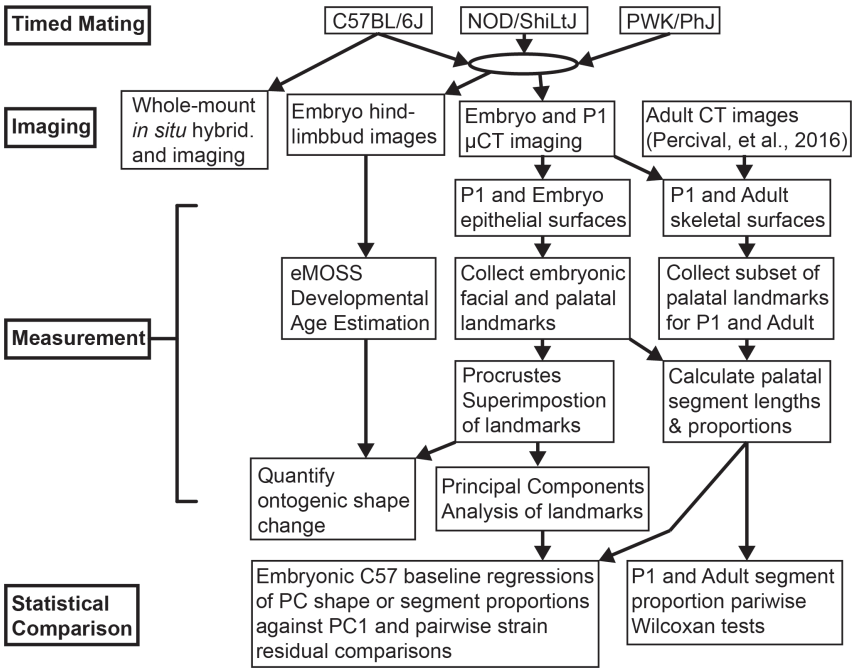

194 Figure 2 - Flowchart illustrating this study's research design

195 **In Situ Hybridization**

196 In situ hybridization was performed as described in Welsh et al., 2018. cDNA probes for
197 *Phospho1* (nucleotides 274–1739 of RefSeq NM_153104), *Runx2* (nucleotides 1275–2704 of
198 RefSeq NM_001271627), *Shh* (full length cDNA clone from A. McMahon, University of
199 Southern California, Los Angeles CA, USA), *Shox2* (nucleotides 870–1603 of RefSeq
200 NM_130458), *Sp7* (nucleotides 431–1715 of RefSeq NM_130458), *Tbx22* (nucleotides 307–

201 1547 of RefSeq NM_013665) were linearized and in vitro transcribed to label with either
202 digoxygenin (DIG) or dintrophenol (DNP). Colorimetric detection of probes used BM purple
203 (dark blue), BCIP (teal), or MagentaPhos (magenta). Minimally, 3-6 embryos per time point
204 were processed for each probe analyzed.
205
206 **DMDD HREM Data**
207 High resolution episcopic microscopy (HREM) data (Geyer et al., 2009) was generated as
208 part of the deciphering mechanisms of developmental disorders (DMDD) program (Wilson et al.,
209 2016) and is available from the BioImage Archive at:
210 https://www.ebi.ac.uk/biostudies/bioimages/studies/S-BIAD490?query=DMDD
211
212 **Embryonic Palatal Segment Growth Trajectories**
213 Developmental Age Estimation
214 Given that common mouse strains vary in gestation length and there is variation in
215 developmental timing within litters, it was necessary to standardize our cross-strain
216 morphometric analysis by embryonic developmental age rather than gestational age.
217 Developmental age was estimated for each µCT scanned embryonic specimen using eMOSS, an
218 application that predicts developmental age from hindlimb bud outlines, based on a previous
219 analysis of C57 mice (Musy et al., 2018). The resulting limb-based estimates of developmental
220 age were reported as days since conception, up to two decimal places. We combined similar
221 developmental age estimates whole- or half-day developmental age categories that include
222 specimens within 0.25 days of their initial eMOSS estimate (Table 1).

223 Additional error may be expected when estimating the developmental age of NOD and
224 PWK embryos using a predictive model built on C57 strain limb bud ontogeny, given the
225 possibility of differences in the correlation of limb and head development between strains.
226 Therefore, we also utilized the first principal component of embryonic head shape variation
227 (PC1), based on the landmark analysis described below, as a proxy for developmental age in
228 some analyses. PC1 score consistently tracked ontogenetic change in facial and palatal shape
229 across strains (see Results).
230
231 Anatomical Landmark Collection
232 All embryo facial and palate landmarks were collected within Meshlab (Cignoni et al.,
233 2008) on minimum threshold-based superficial tissue surfaces (downsampled x2) produced from
234 the μCT images. Landmarks that could be identified consistently in anatomically homologous
235 positions across the embryonic period of facial growth were chosen around the nose and whisker
236 region, the eyes, and along the palate (Fig. 3, Supporting Table 1). The facial landmarks we
237 collected were previously defined to track developmentally homologous structures across
238 multiple stages of facial development (Percival, et al., 2014) and our new set of palatal
239 landmarks were defined similarly. Similar care was taken to define embryonic epithelial tissue
240 palatal landmarks that could be associated with the bony morphology of the P1 and adult mouse
241 upper jaw.
242
243 Prenatal Geometric Morphometric Analysis
244 A Procrustes superimposition-based geometric morphometric analysis was used to
245 quantify the ontogenetic shape change of the palate and face for the embryonic C57 sample and

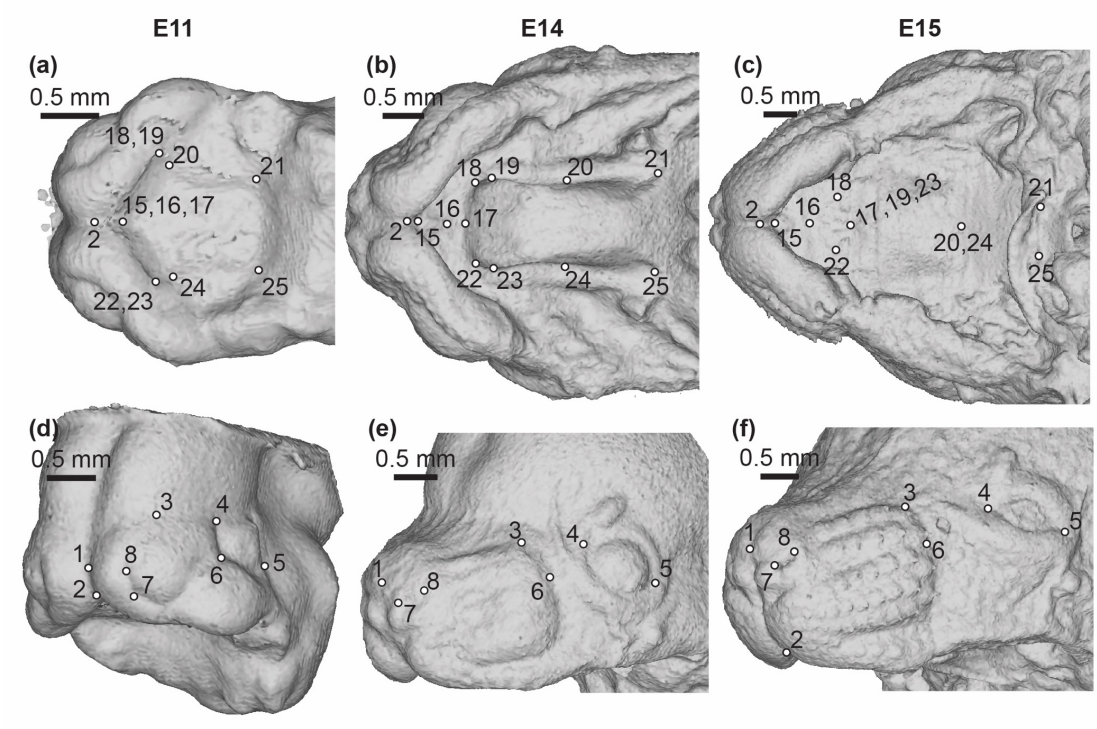

Figure 3 – Anatomically homologous epithelial landmarks - Landmarks collected for the quantification of midfacial and palatal shape across limb based embryonic (E) developmental stages, from (a-c) palatal and (d-f) oblique facial views. Scale bars: 0.5mm. See also Supporting Table 1.

deviations of the NOD and PWK strains from this C57 baseline. The C57 strain was chosen as a baseline because it is the most widely utilized inbred strain for genetic analysis and because it was the strain originally used to train the eMOSS limb bud staging algorithm (Musy et al., 2018). Embryonic specimens with limb-based developmental age estimates between E11 and E15 were included in the embryonic shape analysis (Table 1). We performed a geometric morphometric analysis of facial landmarks using *geomorph* (Adams et al., 2020) and RRPP (Collyer and Adams, 2018) libraries in R Statistical Software (R Core Team, 2021). Generalized Procrustes analysis (GPA) aligned specimen landmark sets by translating, scaling, and rotating their landmark coordinates (reviewed by Zelditch et al., 2012). Embryonic specimen shape analyses were completed using the symmetric component of Procrustes-aligned specimen landmark coordinate variation, assuming that most bilateral shape differences between the left and right

257 sides of a specimen's face are due to random effects associated with developmental noise and
258 tissue fixation (Palmer and Strobeck, 1986). Thus, symmetrized landmark coordinate data were
259 interpreted to represent the facial shape defined by a given inbred strain genotype.

260 The mean facial shape of specimens within each developmental age category were
261 estimated for each strain. Differences between C57 strain age-specific mean shapes were plotted
262 to illustrate typical facial/palatal shape growth trajectories during this important period of
263 secondary palate elongation and midline fusion. A principal components analysis (PCA) was
264 completed to identify the major axes of shape covariation across the embryonic sample. As with
265 most PCAs of ontogenetic series, the first principal component (PC1) was strongly associated
266 with overall specimen size and specimen developmental age. Therefore, we treated it as a proxy
267 for ontogenetic growth and developmental age. C57-specific regressions represented a baseline
268 of overall facial/palatal shape change to which the NOD and PWK specimens were compared.
269 Due to clear inflection points in the slopes of embryonic specimen PC scores when plotted
270 against PC1, segmented linear regressions were completed separately for PC2, PC3, and PC4
271 versus PC1 values for the C57 sample.

272 After removing three NOD specimens with PC1 scores that were substantially lower than
273 the minimum C57 PC1 score that the C57 regression was based on, we predicted PC2, PC3, and
274 PC4 scores from each C57, NOD, and PWK specimen's PC1 score based on the C57 baseline
275 regressions. Then we calculated the PC score residuals of each specimen as the difference
276 between predicted and measured PC scores. We completed Wilcoxon rank sum tests to identify
277 significant genotypic differences for PC2, PC3, and PC4 residual values representing the whole
278 embryonic period at once (i.e. statistical tests were not performed at specific embryonic ages
279 within the sampled age range). A significant difference in mean PC score residual values

between strains was interpreted as a significant difference in the ontogeny of facial shape for that pair of strains.

Prenatal Palate Segment Length

The anterior-posterior length of the three major palatal segments (i.e., primary palate, anterior secondary palate, and posterior secondary palate) were estimated in millimeters from landmark coordinates without superimposition or scaling. To estimate the length of these segments along the anterior-posterior axis of the palate, the mean midline position between bilateral landmark pairs were calculated. Proportional palatal segment lengths were calculated as the length of a single segment divided by the sum of all three segment lengths for a given specimen (Fig. 4).

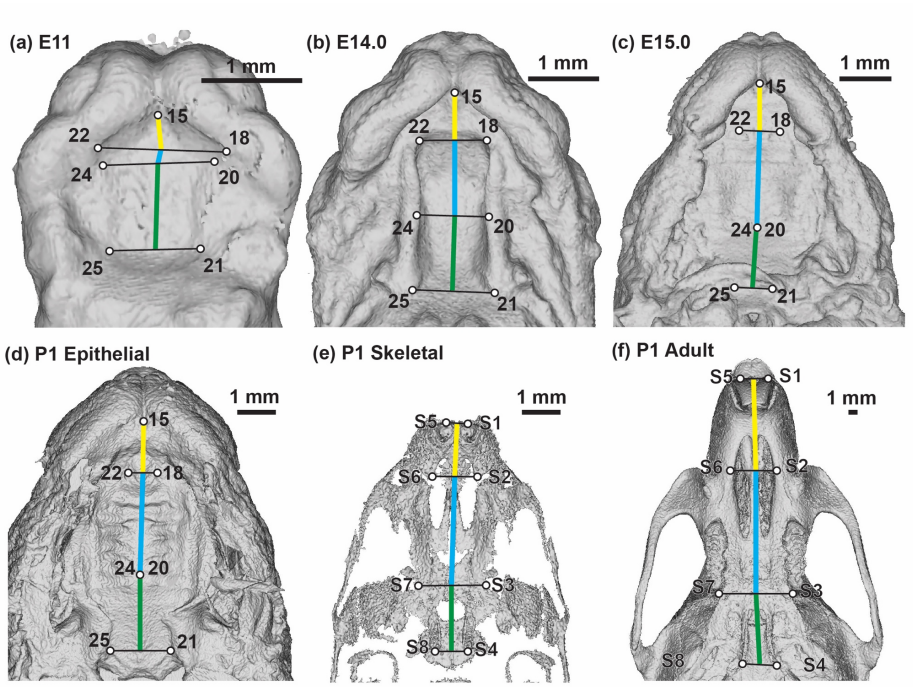

Figure 4 – Palate segment length measurements – Identification of landmarks used to estimate midline lengths of the primary palate (yellow), anterior secondary palate (blue), and posterior secondary palate (green) on (a) E11.0, (b) E14.0, (c) E15.0 epithelial, (d) P1 epithelial, (e) P1 skeletal (after removing some neurocranial and facial bones to help with visualization), and (f) adult skeletal surfaces. Scale bars: 1mm. See also Supporting Tables 1 and 2.

291

292 Small strain-specific sample sizes at multiple limb-based developmental ages meant it
293 was not statistically appropriate to compare proportional palate segment contributions between
294 inbred strains at single developmental ages. Instead, second-degree polynomial regressions of
295 proportional palate segment lengths versus specimen facial shape PC1 score were calculated for
296 the entire C57 embryo sample. Because PC1 score was considered a proxy for developmental
297 age, these regressions define ontogenetic trajectories of palatal segment contributions to overall
298 palatal length, which were used as a baseline for comparison with NOD and PWK proportional
299 segment lengths. After removing three NOD specimens with PC1 scores that were substantially
300 lower than the minimum C57 PC1 score that the C57 regressions were based on, we predicted
301 the proportional length of each palatal segment for all specimens based on the C57 regressions.
302 The residual differences in proportional palatal segment lengths between predicted and measured
303 values representing the whole embryonic period at once were compared across the three strains
304 using Wilcoxon rank sum tests. Statistical tests were not performed at specific embryonic ages
305 within the sampled age range. A significant difference in mean residual values was interpreted to
306 indicate a higher or lower proportional contribution of a given palate segment to overall palatal
307 length, either across the entire embryonic period or during some major portion of this embryonic
308 period.

309

310 **Postnatal Palate Segment Length Comparisons**

311 To determine if embryonic differences in proportional palate segment length remained
312 consistent postnatally and to investigate the degree of correspondence between surface epithelial
313 and skeletal measures of palatal variation, postnatal specimen landmarks were collected on

314 minimum threshold-based surfaces produced from μCT scans. Superficial epithelial surfaces of
315 P1 specimens were produced using Amira (downsampled x2), and epithelial landmarks
316 (Supporting Table 1) were collected within Meshlab (Cignoni et al., 2008).
317 Minimum threshold-based skeletal surfaces of P1 and adult specimens were produced
318 using 3D Slicer (Fedorov et al., 2012) after Gaussian blur image filtering (sigma set to 0.01 for
319 P1; sigma set to 0.02 for adult). We identified skeletal anatomical landmarks that most closely
320 matched the palate segment landmarks defined on surface epithelium (Supporting Table 2).
321 Landmarks were collected for C57 (n=10) and NOD (n=8) P1 specimens and for C57 (n=20),
322 NOD (n=18), and PWK (n=18) adult specimens. Midline palate segment lengths and associated
323 upper jaw bone lengths were measured from mean midline positions of bilateral landmark pairs
324 without scaling or superimposition. Proportional palate segment lengths were calculated as
325 individual segment lengths divided by sum of the three midline palatal segment lengths (Fig. 4).
326 Wilcoxon rank sum tests were used to identify significant differences in proportional palate
327 segment lengths between strains within single age and tissue type categories.
328

329 **Results**

330 **Secondary Palate A-P Growth and Ruga 1's Position at a Facial Growth Center**

331 Close relationships between different anatomical domains underlying midfacial
332 outgrowth are found centered near ruga 1 (& Supporting Fig. 1, red arrowheads). Our embryonic
333 series confirmed that ruga 1 formed within the MxP from a domain of *Shh* expression at the
334 anterior extreme of the nascent secondary palate. As previously shown, other rugae then formed
335 anterior to ruga 1 at the RGZ (Fig. 5c, asterisk) as the anterior secondary palate elongated,
336 anteriorly displacing the primary palate and external nares. A separate domain of *Shh* expression

337 posterior to ruga 1 gave rise to the geschmacksstreifen (gs) and sensory papilla arrayed across
338 the most posterior palate. Our embryonic series also confirmed that ruga 1 is consistently found
339 at the *Shox2/Tbx22* gene expression boundary between the anterior and posterior secondary
340 palates during this critical embryonic period of palatal development (Fig. 5 & Supporting Fig. 1).
341 We identified a previously underappreciated association between ruga 1 and the posterior
342 wall of the nasal capsule. At E11.5, ruga 1 formed adjacent to the primary choanae (Fig. 5a &
343 Supporting Fig. 1a, white arrowheads); the posterior openings of the nasal passages, which

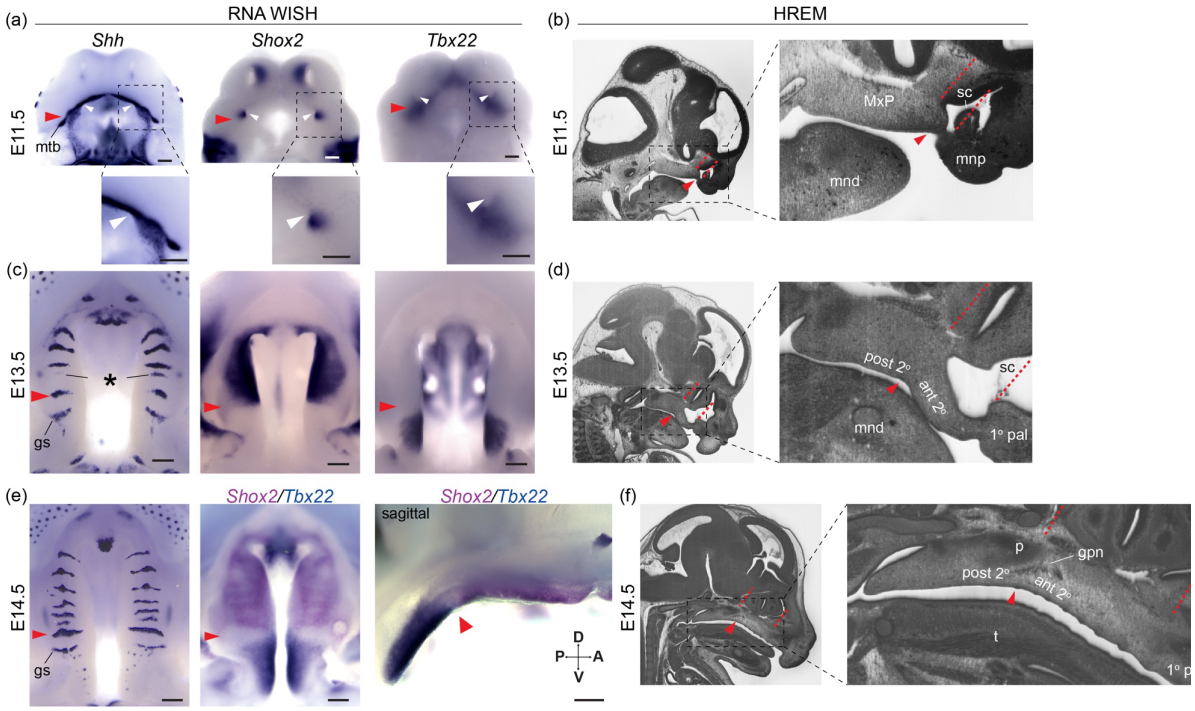

Figure 5 – A-P molecular heterogeneity and anatomical relationships during secondary palate morphogenesis - (a, c, e) RNA WISH for *Shh*, *Shox2*, and *Tbx22* expression, and (b, d, f) sagittal sections of wildtype embryos imaged with high resolution episcopic microscopy (HREM) to provide histological resolution of the primary (1° pal), anterior secondary (ant 2°), and posterior secondary palate (post 2°) relative to surrounding facial structure during midfacial outgrowth at (a, b) E11.5 (c, d) E13.5, and (e, f) E14.5. Throughout midfacial outgrowth, ruga 1 (red arrowheads) marks the shared A-P expression boundary of *Shox2* and *Tbx22* in the anterior and posterior secondary palate, respectively. Double label WISH for *Shox2* (magenta) and *Tbx22* (blue) at E14.5 highlights mutually exclusive anterior and posterior expression domains organized relative to ruga 1 (oral view left, sagittal view right). White arrowheads mark the choanae, black asterisk marks the RGZ. Red dashed lines mark position of coronal planes passing through the primary-secondary palate junction and posterior wall of the nasal capsule to highlight coordinated elongation of the anterior secondary palate and overlying sinus cavity (sc). Regions in dashed boxes of (a) and in HREM images shown enlarged below or to the right, respectively. Additional abbreviations: mandible (mnd), molar tooth bud (mtb), maxillary process (MxP), medial nasal process (mnp), tongue (t), greater palatine nerve (gpn), geschmacksstreifen (gs), palatine (p), posterior domain of *Shh* expression (pd). Scale bars: 250um

344 initially occur at the boundary of primary and secondary palatal segments (Tamarin, 1982).
345 Elongation of the anterior secondary palate then coincided with the formation and expansion of
346 the overlying nasal capsule. As the primary choanae and nasal capsule elongated between E11.5
347 and E15.5, ruga 1 and the posterior wall of the nasal capsule remained in approximately the same
348 coronal plane (represented by position of red dashed lines in Fig. 5b, 5d, 5f and Supporting Fig.
349 1). Ruga 1 was also found coincident with a gross morphological inflection point of the palatal
350 tissue where the anterior secondary palate and overlying nasal capsule exhibited an inferiorly
351 accentuated angle relative to the cranial base, while the posterior secondary palate did not (Fig.
352 5d-f, Supporting Fig. 1).

353 The greater palatine neuro-vascular bundle was also consistently associated with ruga 1
354 across this embryonic period. The greater palatine nerve and artery were found entering the
355 palatal shelves from a location immediately dorsal to ruga 1 at E12.5 and this spatial relationship
356 was maintained until the greater palatine foramen formed by the articulation of maxilla and
357 palatine bones around the palatine neuro-vascular bundle at the maxillary-palatine suture (Fig.
358 5f, Supporting Fig. 1). In combination, the consistent associations between ruga 1, the anterior-
359 posterior secondary palate boundary, the posterior margin of the nasal capsule, and greater
360 palatine neurovascular bundle suggested that these features are positioned at a proximal source
361 of directional growth that the elongating anterior secondary palate and nasal capsule extend away
362 from between E11.5 and E15.5.

363 A complementary 3D morphometric analysis of midfacial and palatal epithelial
364 landmarks was used to quantify the integrated morphogenetic processes occurring during this
365 critical developmental period. The first major principal axis of facial shape variation (PC1) for
366 all limb bud staged E11-E15 specimens represented 70% of shape variance and was associated

with general ontogenetic growth during this time window, as illustrated for the C57 sample (Fig. 6) and for all three inbred strains (Supporting Fig. 2). Additional principal axes of variation for C57 embryos suggested shifts in the direction of ontogenetic shape changes over developmental time, with one inflection noted along PC2 (Fig. 6a), two along PC3 (Fig. 6b), and three along PC4 (Fig. 6c). Average developmental age category shape differences were illustrated as landmark specific ontogenetic shifts in palate shape (Fig. 7) and overall midfacial shape (Supporting Fig. 3).

Between developmental stages E11 and E15, each of the three major palatal segments

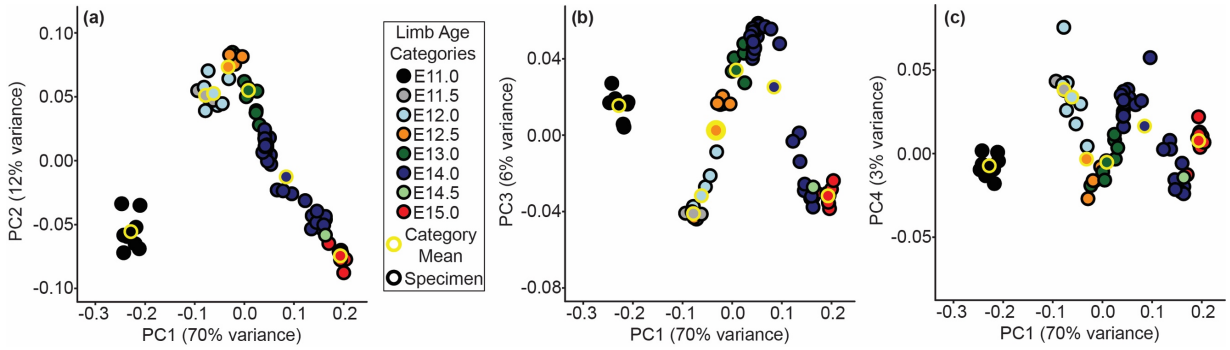

Figure 6 – Major axes of embryonic facial shape variation - C57 embryo specimens plotted along the (a) first and second principal component axes of shape (i.e., PC1 and PC2), (b) along PC1 and PC3, and (c) along PC1 and PC4. Circle color indicates the limb based developmental age categories of each specimen, with the yellow bordered circles indicating the mean PC scores for the C57 mice of that age category. The proportions of facial shape variance associated with each principal component are provided. The principal component axes were estimated from the full sample of E11-E15 developmental age embryos, including C57, NOD, and PWK samples, although only C57 samples are plotted in this figure. The same plot, but incorporating all three inbred strains is available as Supporting Figure 2.

grew in length, but the anterior secondary palate grew proportionally more than the primary palate and posterior secondary palate (Figs. 5 & 7). The primary palate represented ~20% of the total palate length, the anterior secondary palate ~20%, and the posterior secondary palate ~60% for C57 embryos soon after the start of A-P palate elongation. After E12.5, secondary palate length (relative to overall facial size) increased noticeably with each developmental stage. By the time of midline palatal fusion, the primary palate represented ~25% of palate length, the anterior

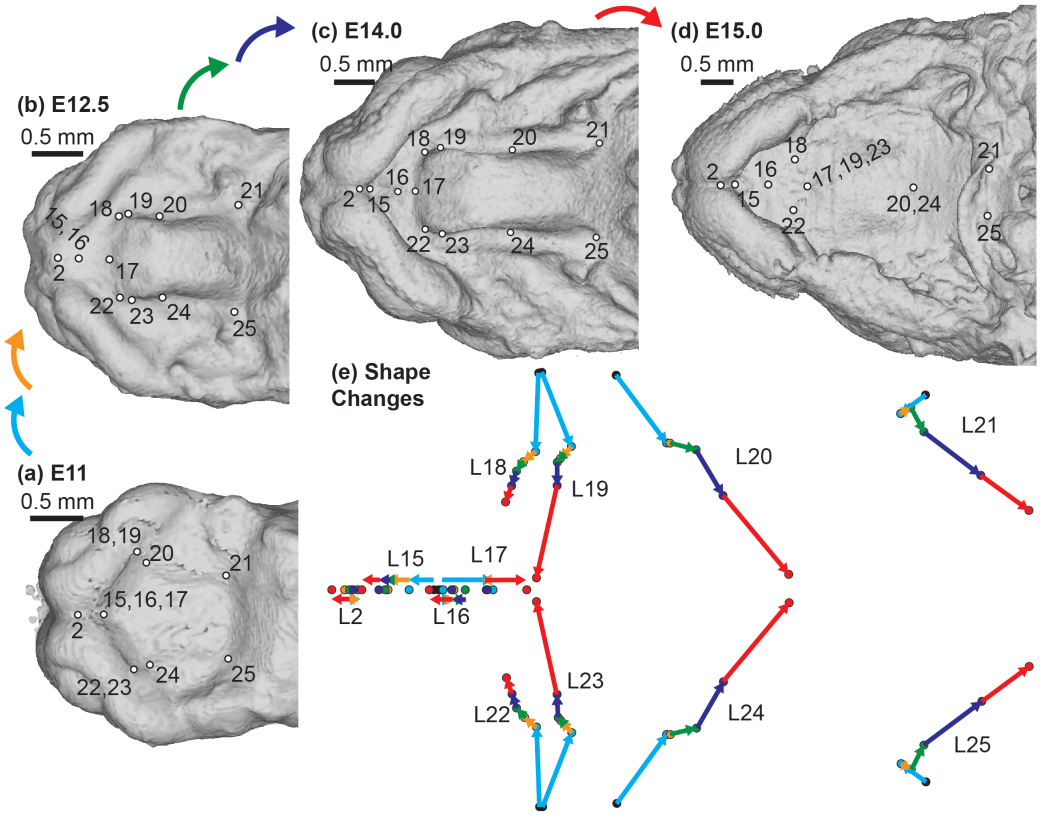

Figure 7 – C57 palatal landmark growth trajectories – The positions of palatal landmarks are identified on representative C57 specimens at limb-derived developmental ages (a) E11, (b) E12.5, (c) E14, and (d) E15. (e) The average palatal landmark positions are plotted for each developmental age category that had more than one C57 specimen. These landmark positions represent palatal shape after the removal of overall facial scale during Procrustes superimposition. The arrows indicate the trajectory of shape change for each landmark between ages. Black=E11; Light Blue = E12; Orange = E12.5; Green = E13; Dark Blue = E14; Red = E15. Scale bars: 0.5mm

secondary palate represented >40%, while the posterior secondary palate represented <35%. Therefore, between E11 and E15, the proportional contribution of the primary palate increased by a quarter while posterior secondary palate contribution decreased by nearly a third. Strikingly, the proportional contribution of the anterior secondary palate to overall palate length doubled during this period.

Segmental Differences in Skeletal Specification, Differentiation, and Growth During Secondary Palate Morphogenesis

We performed a WISH analysis of *Runx2*, *Sp7*, and *Phospho1* expression () alongside double labeled WISH of *Shh* and *Sp7* between E12.5 and E15.5 () to characterize bone specification and differentiation in relation to A-P growth dynamics of secondary palate segments. The position of rugae, which provided an ordered set of temporally specific

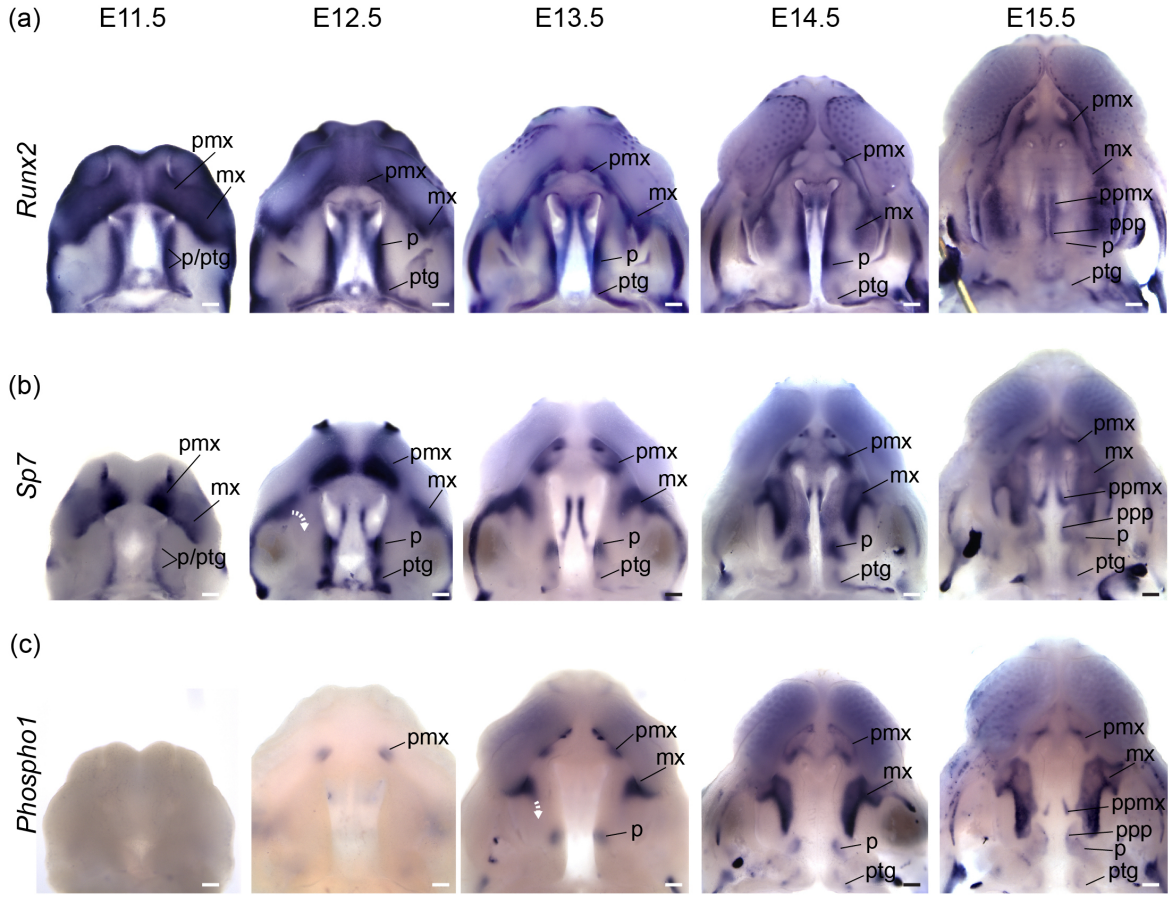

Figure 8 – Segmental organization of skeletal specification and growth during A-P morphogenesis of the midface – WISH time course for (a) *Runx2*, (b) *Sp7*, and (c) *Phospho1* between E11.5 and E15.5. Expression of *Runx2* in osteoprogenitors highlights facial domains with osteogenic potential during midfacial morphogenesis. Expression of *Sp7* and *Phospho1* in committed and differentiating osteoblasts delineates the growth dynamics of individual skeletal anlagen during midfacial morphogenesis. Curved white dashed arrows in (b) and (c) indicate medial expansion of maxillary anlage. Abbreviations: maxilla (mx), palatine (p), premaxilla (pmx), pterygoid (ptg), palatal process of the maxilla (ppmx), palatal process of the palatine (ppp). Scale bars: 250um

393 anatomical features, allowed for the identification of previously unappreciated associations
394 between the palatal segments and developing palatal bones.
395 Broad *Runx2* expression in early facial prominences included osteogenic domains (e.g.,
396 premaxilla within the primary palate) and later became more restricted to regions adjacent to the
397 molar tooth bud and medially along the adjoining palatal shelves (Fig. 8a). Osteoblast expression
398 of both *Sp7* and *Phospho1* more precisely delineated the morphology of the emerging midfacial
399 skeleton (Fig. 8b-c). Palatal processes of the maxilla and palatine bones formed within the
400 medial region of the elevated palatal shelves, a domain that maintained high levels of *Runx2*
401 expression during secondary palate growth (Fig. 8a), suggesting maintenance of a less
402 differentiated osteoprogenitor population until palatal elevation and fusion was complete.
403 At E11.5, *Sp7* was strongly expressed in bilateral domains within the mnp of the forming
404 primary palate. Between E12.5 and E15.5, presaging premaxilla morphology, *Sp7* expression
405 formed a cup-like region surrounding the developing incisors (Fig. 8b). *Phospho1* was first
406 observed in the forming premaxilla at E12.5 (Fig 8c), reflecting a temporal lag between initial
407 osteoblast commitment and later differentiation. The premaxilla acquired its characteristic adult
408 morphology within the primary palate segment in which it was initially specified.
409 Within the secondary palate, this simple developmental sequence was repeated for the
410 palatine and pterygoid bones within the posterior secondary palate, but development of the
411 maxilla within the anterior secondary palate was unique. At E11.5, *Sp7* expression in the MxP
412 was observed in two domains. The anterio-lateral domain, which abutted the point of fusion with
413 the mnp (i.e., the primary palate) and extended laterally away from the oral cavity and choanae,
414 corresponded to the maxillary anlage. The posterior domain that spanned the length of the

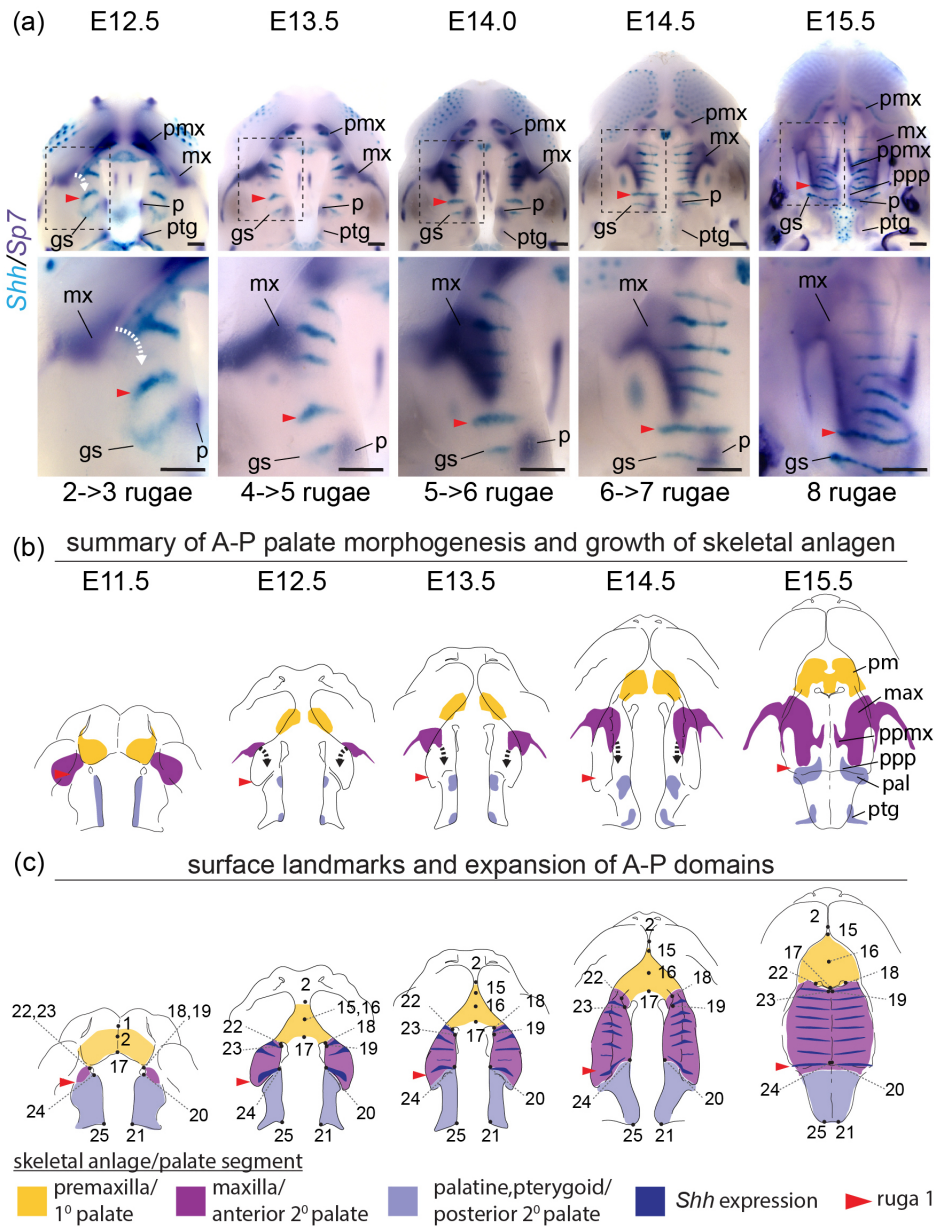

Figure 9 – Double label RNA WISH time course for *Shh* (cyan) and *Sp7* (dark purple) between E12.5 and E15.5 - (a) Expression of *Sp7* in committed and differentiating osteoblasts delineates the growth dynamics of individual skeletal anlagen and *Shh* expression in rugae provides a temporally ordered set of A-P landmarks (regions in dashed boxes enlarged below). (b) Summary model of skeletal growth dynamics during midfacial outgrowth. Growth of the premaxilla (yellow) and palatine (pale blue) anlagen towards their characteristic shape occurs largely at the site of initial specification. Following initial specification external to the oral cavity, the maxilla (purple) grows into the anterior of the anterior secondary palate (curved white and black dashed arrows in a and b, respectively) towards the position of ruga 1 (red arrowhead) and palatine as expansion of the anterior secondary palate (double headed red arrow) separates the primary and posterior secondary palate. (c) Summary of the position of epithelial landmarks (see also Fig. 3) selected to capture segmental growth dynamics of the primary palate (yellow) and anterior secondary palate (purple) and posterior secondary palate (pale blue) during midfacial outgrowth. Abbreviations: geschmacksstreifen (gs), maxilla (mx), palatine (p), premaxilla (pmx), pterygoid (ptg), palatal process of the maxilla (ppmx), palatal process of the palatine (ppp). Scale bars: 250um

forming secondary palate, from the anterior limit abutting the choanae to the posterior-most

416 palatal edge, gave rise to the palatine and pterygoid anlagen.

417 The antero-lateral domain of *Sp7* expression adjacent to the primary palate was initially
418 external to the secondary palate at the site of the future zygomatic plate. However, this
419 expression domain later expanded medially (E12.5-E13.5) and then posteriorly (E13.5-E15.5)
420 within the growing anterior secondary palate (white curved dashed arrows in Fig. 8b). This
421 expansion occurred after initial A-P growth of the anterior secondary palate and formation of 3-4
422 rugae anterior to ruga 1, suggesting that it is coupled with RGZ growth dynamics (Fig. 9a). The
423 fact that *Phospho1* expression closely followed *Sp7* spatial dynamics further supported the idea
424 that these *Sp7* expression patterns represent maxillary bone anlagen formation and expansion
425 (white curved dashed arrow in Fig. 8c). The maxillary anlage continued growing posteriorly
426 towards ruga 1 concomitant with rugae formation (white and black curved dashed arrows in Fig.
427 9a-b), within the elongating secondary palate.

428 The posterior domain of *Sp7* expression that initially spanned the length of the secondary
429 palate at E11.5 was displaced posteriorly by expansion of the anterior secondary palate between
430 E12.5 and E15.5. During this period, it separated into two subdomains. The anterior subdomain
431 remained associated with the posterior wall of the nasal capsule and gave rise to the palatine
432 bone, while the posterior subdomain formed both the medial and lateral pterygoid processes (Fig.
433 8b-c). Ruga 1 and the palatine anlage initially formed at the anterior extent of the secondary
434 palate at E11.5 and maintained proximity to each other throughout palatal development even as
435 both structures were displaced posteriorly (Fig. 9a).

436 The palatine and pterygoid anlagen grew to acquire their characteristic adult morphology
437 within the posterior secondary palate segment where their precursor domains were initially
438 specified, mirroring premaxillary anlagen formation within the primary palate. This differs from

439 growth of the maxillary anlage that was initially specified external to the secondary palate at the
440 site of the future zygomatic plate and only later extended into the anterior secondary palate,
441 following a period of initial elongation, to give rise to the majority of the maxillary bone.
442 These results indicated that the posterior portion of the secondary palate and its
443 associated anlage were present within the secondary palate at the onset of its morphogenesis at
444 E11.5, while the anlage associated with the anterior secondary palate (i.e. the maxilla) did not
445 contribute substantially to the secondary palate until later (Fig. 9b). They also indicated that the
446 eventual meeting of the maxilla and palatine anlagen was an asymmetric process achieved
447 predominantly by posterior growth of the maxilla towards the palatine (white and black curved
448 dashed arrows in Fig. 9-b). By E15.5, the maxilla and palatine anlagen met to form the
449 maxillary-palatine suture subjacent to ruga 1 (see also Supporting Fig. 1).
450 Our results collectively revealed that the segmental relationship between three palatal
451 regions and associated bone anlagen remained consistent throughout the period of palatal
452 elongation, although the maxillary anlage was not present within the anterior secondary palate
453 until part way through this period. Importantly, these results also highlighted the previously
454 unappreciated correlation of maxillary growth to rugae formation as well as to the greater
455 proportional expansion of the anterior secondary palate between E11.5 and E15.5 (summarized
456 in Fig 9C).
457
458 **Interstrain Comparisons of Facial and Palatal Growth**
459 We completed a morphometric comparison of C57, NOD, and PWK strain embryonic
460 midfacial shapes and a comparison of proportional palatal segment lengths across embryonic and
461 postnatal stages to test the hypothesis that early differences in palatal segment growth contribute

462 to variation in adult midfacial shape, including strain specific differences in proportional bone
463 contributions to upper jaw length.

464 Because developmental speed varies between mouse strains and within litters, we
465 standardized our cross-strain ontogenetic analysis using limb bud outline-based embryonic
466 developmental age rather than gestational age. Limb bud developmental ages correlated strongly
467 with the number of days after plug identification for each strain. Though the correlation
468 coefficients for C57 mice (0.98), NOD (0.93) and PWK (0.90) were high, there was a larger
469 difference between these two embryonic age estimates for our PWK samples. The C57 specimen
470 limb-based developmental ages were an average of 0.26 days younger than our copulatory plug
471 estimates, while NOD and PWK limb ages were an average of 0.30 days and 1.09 days younger,
472 respectively. The major divergence for PWK was likely driven by a slower speed of embryonic
473 development in this wild-derived strain compared to the two common lab strains (Murray et al.,
474 2010). Even so, standardization by developmental age should allow for improved direct
475 comparisons between embryos of all strains.

476 We compared the midfacial shape of NOD and PWK specimens with C57 specimens
477 along the principal axes of facial shape variation. This comparison indicated that mice with
478 similar limb-based developmental age estimates tended to fall near each other along the first and
479 second principal components, regardless of strain. As these axes represented 82% of facial shape
480 variance across our sample, all mouse strains displayed major similarities in ontogenetic shape
481 change across this period (Supporting Fig. 2a). However, across ontogenetic time (as represented
482 by PC1 score) NOD and PWK specimens had significantly lower PC3 values compared to the
483 C57 baseline, based on a comparison of regression residual values representing the entire

484 sampled embryonic period (Fig. 10b). PWK specimens also had significantly lower PC4 values

485 (Fig. 10c).

486 We visualized how these identified significant differences in PC3 or PC4 scores were

487 reflected within facial and palatal morphology by comparing shapes represented at the minimum

488 and maximum end of these major shape axes (Fig. 11), with strain representative whole mount

489 (Supporting Fig. 4) and μCT surface (Supporting Fig. 5) images provided for reference. A

490 minimum PC3 score was associated with the two nostril landmarks (LM7 & 8) being relatively

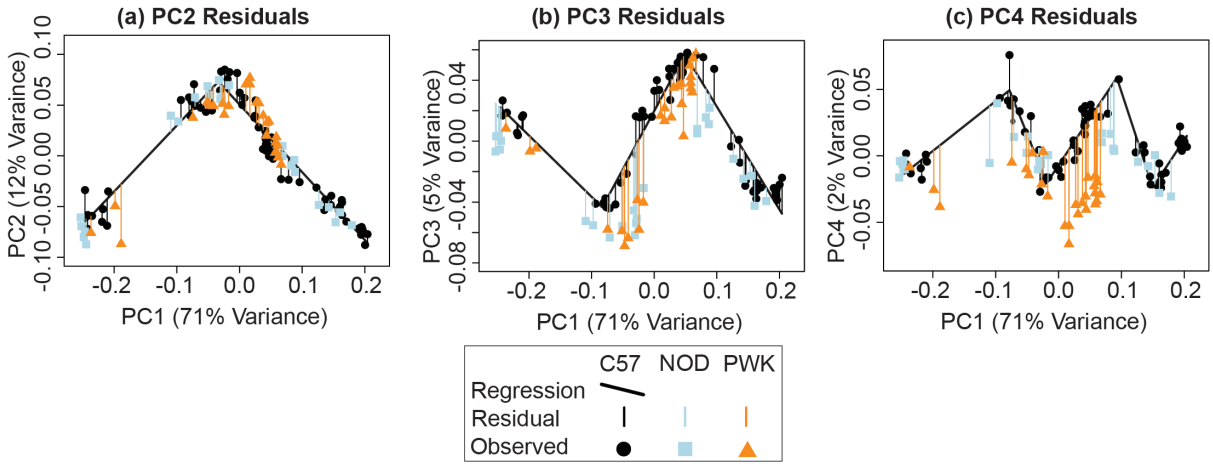

Figure 10 – Specimen PC score residuals – The principal component (PC) score residuals for each specimen, relative to the scores predicted from C57 strain specific segmented linear regressions of (a) PC2, (b) PC3, and (c) PC4 on the specimen's PC1 score. In this way, the C57 facial shape growth trajectory serves as a baseline with which to compare the shape of NOD and PWK specimens, based on the fact that the PC1 axis is strongly associated with facial shape ontogeny from developmental age E11 to E15.

491 distant in the superior/inferior and lateral directions. Lower PC3 score was also associated with

492 relative proximity of the posterior whisker margin (LM6) to the anterior canthus (LM4) (h).

493 Within the palate, lower PC3 scores were associated with a relatively medial anterior secondary

494 palatal shelf, suggesting more medial palatal outgrowth (proportional to overall palatal length) at

495 a given developmental stage (Fig. 11b). The superior-inferior position of the palatal landmarks

496 indicated that the secondary palate was more highly angled (less flat) for specimens with low

497 PC3 scores (Fig. 11e). Because of their generally lower PC3 scores, we anticipated more vertical

498 nostrils in NOD and PWK mice with more highly angled palatal shelves in greater medial

499 proximity to each other, when compared to C57 mice within a given developmental age.

500 A minimum PC4 score was associated with the whole nasal region (LM1, LM8) being

501 positioned more inferiorly and the posterior edge of the whisker region (LM3, LM6) more

502 superiorly when compared to the other facial and palatal features (Fig. 11i, Supporting Figs. 4 &

503 5). Within the palate, a low PC4 score was associated with a relatively anterior location of ruga 1

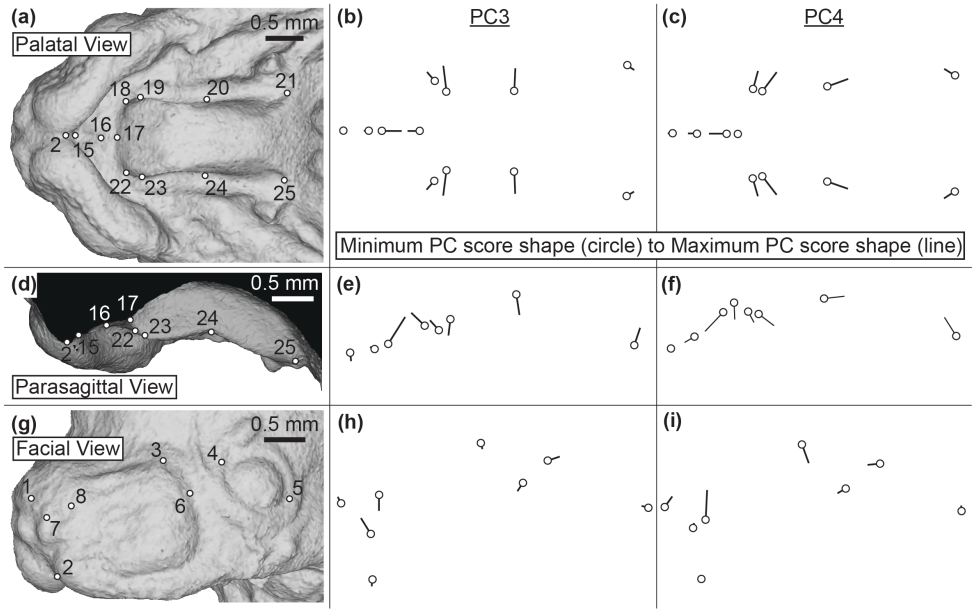

Figure 11 – Facial shape variation associated with PC3 and PC4 – Representation of the pattern of shape variation associated with the third major axis and fourth major axis of embryonic facial/palatal shape variation, from (a-c) palatal, (d-f) parasagittal, and (g-i) facial views. Superficial tissue landmarks are identified on an example E14.5 specimen to assist with interpretation of the landmark vectors that represent differences in minimum (circle) and maximum (end of line) PC scores. See Supporting Fig. 2 for a plot of embryonic specimens along these major axes of embryonic shape variation. Scale bars: 0.5mm

504 between anterior and posterior secondary palate (LM20 & 24) and a relatively posterior position

505 of the posterior edge of the posterior secondary palate (LM21 & 25 within Fig. 11c). Low PC4

506 scores were also associated with more medially positioned anterior secondary palate landmarks

507 that are closer to the boundary with the primary palate. Because of their generally lower PC4

508 scores, this suggested that PWK embryos display a relatively low superior nasal region, a

509 medially expanded anterior secondary palatal shelf with a relatively short anterior secondary

510 palate and relatively long posterior secondary palate, when comparisons are made within a given
511 developmental age.
512 A comparison of embryonic palatal segment lengths (Fig. 4a-c) across C57, NOD and
513 PWK samples indicated that all three mouse strains display parallel ontogenetic changes 1) in
514 overall palatal length and 2) in the proportional contributions of palatal regions to overall palatal
515 length during the period of early palatal morphogenesis (, Supporting Fig. 6). This includes
516 generally increased proportional contributions of the anterior secondary palate and decreased
517 proportional contributions of the posterior secondary palate between E11 to E15, as described
518 above for C57 mice. However, small but significant differences in palatal segment proportions
519 between mouse strains were identified within a comparison of proportional palatal segment
520 length versus facial shape PC1 score (a proxy for developmental age). These comparisons were
521 completed based on regression residuals representing the entire sampled embryonic age range
522 and were not completed at specific embryonic ages. The NOD and PWK primary palate
523 proportional length residuals were significantly lower than for C57 (p-values: 0.012 (NOD vs
524 C57), <0.001 (PWK vs C57)) (Fig. 13a), while they also had significantly higher posterior
525 secondary palate residuals than C57 (p-values <0.001) (Fig. 13c). This indicated that the primary
526 palate contributed relatively less and the posterior secondary palate contributed proportionally
527 more to total embryonic palate length in these two mouse strains, although visual assessment
528 suggested these differences may not be apparent at the earliest measured developmental ages
529 (Fig. 12) or for specimens with the lowest PC1 scores (Supporting Fig. 6). Significantly lower
530 anterior secondary palate residuals for NOD and PWK (p-values: 0.029 (NOD vs C57), 0.023
531 (PWK vs C57)) indicated that the anterior secondary palate represented a lower proportion of the
532 total palate length within these strains (Fig. 13b), although these differences seemed less

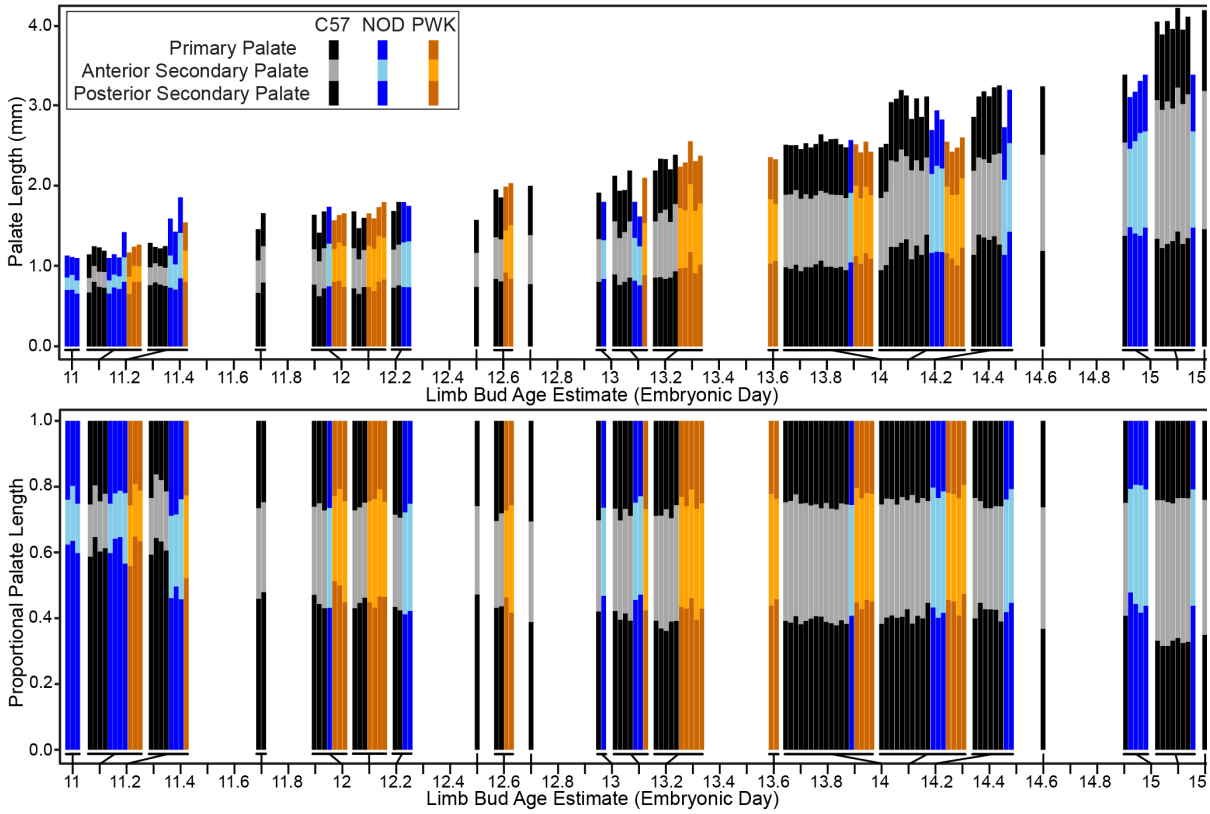

Figure 12 – Embryonic palate segment length across ontogeny – The midline projected strain-specific mean lengths of the primary palate, anterior secondary palate, and posterior secondary palate, for all E11-E15 specimens binned into 0.1 day limb bud derived developmental age categories and sorted by genotype. Raw length values (in millimeters) are presented above, while palatal segment length relative to overall midline palate length are presented below.

pronounced than those noted for the other two segments (Fig. 12, Supporting Fig. 6). Taken together, these trends suggested that C57 mice typically had proportionally longer primary palates and proportionally shorter posterior secondary palates than NOD and PWK mice during this embryonic period, with a trend towards longer anterior secondary palates by the time of medial palatal shelf fusion (Fig. 13).

Interstrain Comparisons of Postnatal Palatal Segments

We compared C57 and NOD proportional palatal segment lengths at P1 based on epithelial surface landmarks and skeletal landmarks of associated bony elements. Based on the

542 epithelial surface landmarks (Fig. 4d), C57 had a proportionally shorter anterior secondary palate
543 and a proportionally longer posterior secondary palate (p-values <0.01) than NOD at P1 (Fig. 14;
544 Table 2). This differed from the embryonic pattern where C57 specimens generally displayed
545 proportionally shorter posterior secondary palates than NOD specimens. The significant
546 differences in epithelially-measured proportional segment contributions between NOD and C57
547 mice at P1 appeared largely based on differences in the measured length (in mm) of the posterior
548 secondary palate (Fig. 14).

549 A comparison of proportional palatal bone lengths in P1 samples (Fig. 4e) indicated that
550 C57 has a proportionally shorter premaxilla (associated with primary palate) and proportionally
551 longer palatine/pterygoid bones (associated with posterior secondary palate) (p-values <0.01)
552 than NOD (Fig. 14; Table 2). A similar comparison of proportional palatal bone lengths (Fig. 4f)
553 in 8-12 week old adult specimens of all three strains revealed that the premaxillary (primary
554 palate) contribution to total palate length is significantly lower in PWK (p-value: < 0.001) and

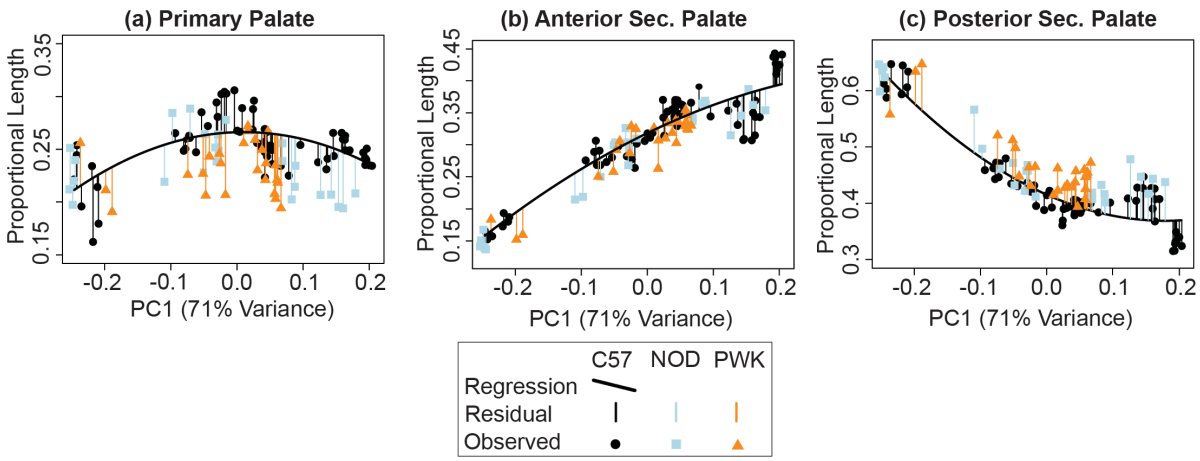

Figure 13 - Specimen palate segment length residuals – The proportional contributions of each palate length segment (shapes), as compared to the proportional contributions predicted from C57 strain specific linear regressions (curved lines) of proportional (a) primary palate, (b) anterior secondary palate, and (c) posterior secondary palate midline lengths versus the specimen's PC1 score. Vertical lines represent the residual of each specimen from C57 regression. In this way, the C57 palatal segment growth trajectory serves as a baseline that NOD and PWK specimens were compared to, based on the fact that the PC1 axis is strongly associated with facial shape ontogeny from E11 to E15.

555 NOD (p-value: 0.044) compared to C57, with the opposite true for the maxillary (anterior
556 secondary palate) portion of the palate (p-values: < 0.001) (Fig. 14). The palatine/pterygoid
557 (posterior secondary palate) portion was proportionally shorter in PWK and NOD when
558 compared to C57 (p-values: < 0.001) (Fig. 14). The PWK average proportional measures of
559 premaxilla and maxilla showed a more extreme divergence from C57 than in the NOD mouse
560 comparison.

561 Overall, there were some ontogenetic changes in how strains differed in proportional
562 palate lengths, either between the embryonic period and P1 or between P1 and adulthood. NOD
563 and C57 showed parallel changes in palatal bone contributions across the postnatal period, where
564 the posterior secondary palate contribution remained fairly stable (~27-29%), but the primary
565 palate contribution increased from ~24% to ~32% and the anterior secondary palate contribution
566 decreased from ~47% to ~40-42% (Fig. 14; Table 2). During the postnatal period, the entire
567 mouse and its palate grew substantially, but premaxilla growth contributed more than the maxilla
568 growth to overall postnatal palatal elongation. Although the A-P growth of the anterior
569 secondary palate was a critical driver for midfacial growth between E11.5 and E15.5, outgrowth
570 of the premaxilla plays a larger role in postnatal midfacial outgrowth.

571

572 **Discussion**

573 Our results provided a multifaceted characterization of 1) normal murine midfacial
574 growth dynamics within the secondary palate and upper jaw bones during the earliest stages of
575 palatal growth and 2) subsequent changes in upper jaw bone proportions in newborn and adult
576 mice. By tracking the position of the RGZ, sequential palatal rugae formation, and palatal bone
577 precursor populations across the earliest phases of palatal A-P elongation, our results illustrated

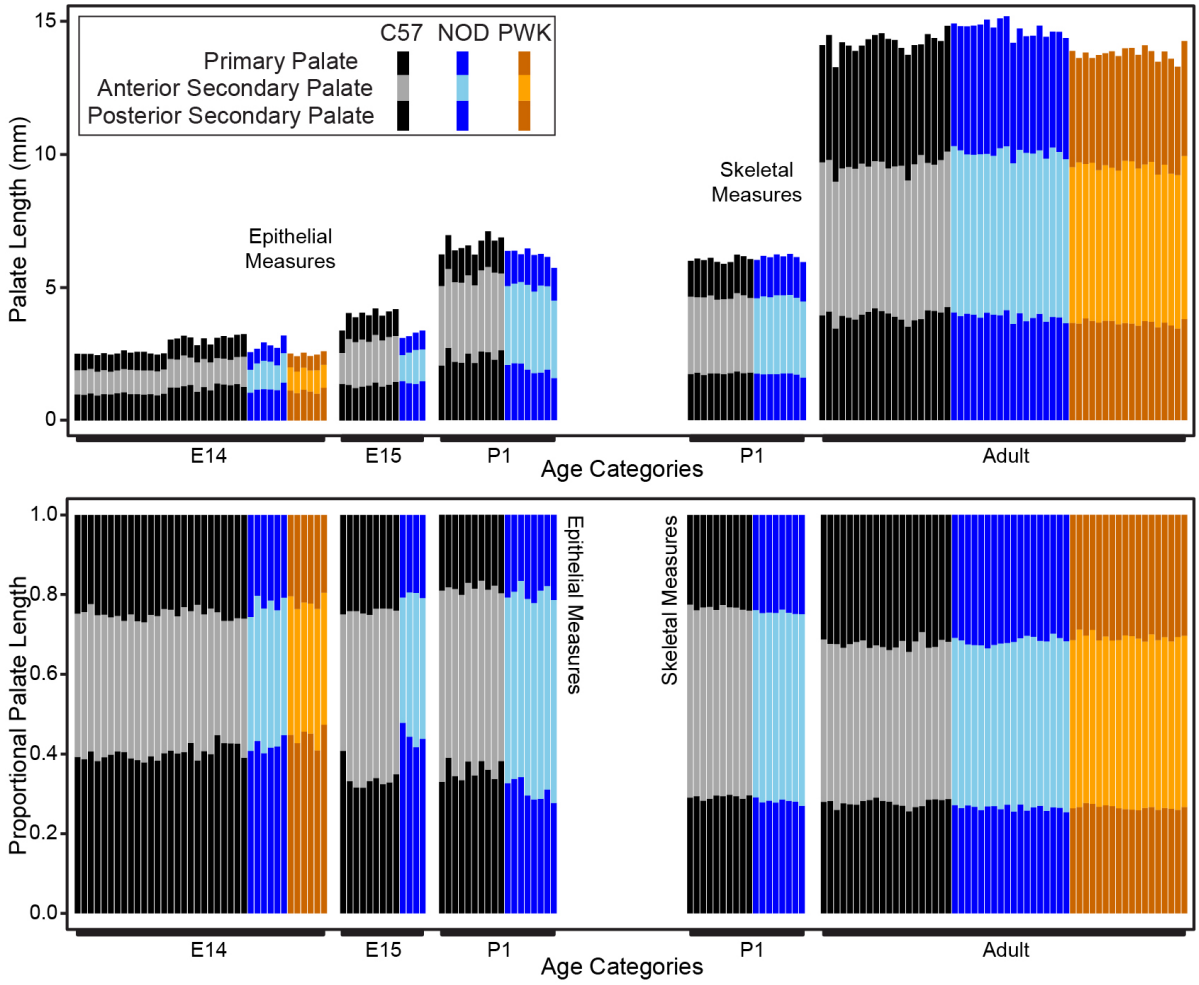

Figure 14 – Interstrain comparisons of palate segment lengths in older specimens – The midline projected lengths of the primary palate, anterior secondary palate, and posterior secondary palate, based on epithelial landmark measures for all specimens of limb based developmental stages E14 and E15, as well as for P1 specimens. Analogous length measures of primary palate derived premaxilla, anterior secondary palate derived maxilla, and posterior secondary palate derived palatine/pterygoid bones are presented for all P1 and adult specimens. Raw length values (in millimeters) are presented above, while palatal segment length relative to overall midline palate length are presented below.

that the first-formed palatal ruga (i.e., ruga 1), which sits at an important border of regulatory gene expression is coincident with important nasal, neurovascular and palatal structures throughout early midfacial development. For example, ruga 1 represents a consistent morphological boundary between the presumptive maxilla of the anterior secondary palate and the presumptive palatine and pterygoid bones of the posterior secondary palate. This association suggested that the process of rugae morphogenesis is coupled to maxillary osteogenesis during

584 anterior secondary palate expansion and that ruga 1 approximates the future position of the
585 maxillary-palatine suture from the time of its formation.
586 Our ontogenetic comparison of epithelial and skeletal palatal anatomy across three mouse
587 strains identified small, but significant strain-specific differences in early palatal morphogenesis
588 and normal midfacial outgrowth. These differences provide a useful foundation for
589 understanding the impact of background genetic effects on facial shape and elongation.
590 However, embryonic differences in palatal segment proportions did not match adult strain-
591 specific differences in the contributions of the premaxilla, maxilla, and palatine/pterygoid bones
592 to upper jaw length.
593
594 **Normal Upper Jaw and Palatal Elongation**
595 It is well known that A-P elongation of the palate is a necessary component of the
596 integrated processes of midfacial outgrowth. However, within mammals, we previously lacked a
597 detailed picture of the earliest spatiotemporal dynamics of intramembranous midfacial skeletal
598 specification and differentiation within the context of the surrounding palatal segments and rugae
599 formation. Our combined whole mount gene expression and morphometric analysis indicated
600 that the relationship between three longitudinal palate segments and associated upper jaw bones
601 was already established during the earliest phases of palatal morphogenesis. These results
602 illustrated the substantial contribution of embryonic anterior secondary palate elongation to
603 overall palate length in mice and likely in other mammals. Anterior secondary palate elongation
604 was also directly associated with rugae formation at the RGZ and elongation of the maxillary
605 bone primordium.

606 Beyond verifying that ruga 1 forms at an important gene expression boundary between
607 the anterior and posterior secondary palate, our results clarified that ruga 1 represented a stable
608 morphological boundary positioned near the future maxillary-palatine suture, as opposed to the
609 alternate hypothesis that it is positioned between hard and soft palate (Pantalacci et al., 2008).
610 Ruga 1 formed at the earliest stages of anterior secondary palate elongation, then maintained a
611 position at the anterior edge of the palatine bone anlage as it was posteriorly displaced by
612 expansion of the anterior secondary palate. Anterior to ruga 1, the maxillary bone osteogenic
613 population expanded from the site of initial specification (i.e. the zygomatic plate) into the
614 secondary palate after ruga 1 was posteriorly displaced during anterior secondary palate
615 elongation. Given that the secondary palate initially only contained osteogenic domains of the
616 posterior secondary palate (palatine and pterygoid precursors), these results suggested that
617 cellular cues in the proximity of ruga 1 may initially inhibit maxillary bone formation within the
618 secondary palate. Additionally, expansion of the palatal portion of the maxillary anlage was
619 uniquely associated with RGZ dynamics and anterior secondary palate elongation, suggesting
620 that RGZ morphogenesis plays a major role in determining the proportional contribution of the
621 maxilla to the upper jaw within a broad evolutionary context. This hypothesis could be tested
622 within an evo-devo context by characterizing variation in palatal *Shh* expression between
623 mammals and avians that have drastic differences in maxillary morphology, including an
624 obligate avian cleft palate. Alternatively, it could be dissected genetically via analysis of *Shh*
625 expression and rugae morphogenesis in mice with altered A-P skeletal patterning, such as the
626 *Pbx* CNCC mouse mutants (Welsh et al., 2018).
627 Differences in upper jaw suture anatomy may also be related to segmental differences in
628 early bone growth. The premaxilla and maxilla were specified in adjacent tissue domains that

629 maintained close apposition throughout palate morphogenesis, suggesting equal contributions to
630 the formation of the premaxillary-maxillary suture. Conversely, the palatal portion of the maxilla
631 grew posteriorly towards the palatine anlage at ruga 1, suggesting that maxillary growth (and
632 likely RGZ dynamics) played a larger role than palatine growth in determining maxillary-
633 palatine suture position. Different growth dynamics at these sutures may lead to a more vertical
634 premaxillary-maxillary suture versus a more oblique maxillary-palatine suture with substantial
635 A-P overlap of the maxilla and palatine bones.

636 Because suture formation provides a critical niche for facial skeletal progenitors (Zhao et
637 al., 2015), the way palatal segments contribute to palatal sutures may contribute to variation in
638 postnatal dynamics of midfacial growth and remodeling (Enlow and Bang, 1965; Kurihara et al.,
639 1980; Sarnat, 1997; Martinez-Maza et al., 2013; Vora et al., 2015; Maga, 2016). The widespread
640 presence of Gli1+ mesenchymal stem cells and nascent bone within the adult maxillary-palatine
641 suture and the maxillary bone, but not in the palatine bone (Luo et al., 2019) provides further
642 support for this hypothesis. Given the established role of calvarial sutures in directing postnatal
643 craniofacial bone growth, further comparisons of osteoprogenitor dynamics during premaxillary-
644 maxillary and maxillary-palatine suture formation are warranted.

645

646 **Palatal Growth as a Basis for Morphological Variation**

647 Given its central contribution to total palatal elongation, variation in RGZ regulated A-P
648 growth of the anterior secondary palate may contribute substantially to the range of prognathism
649 observed amongst mammals (Young et al., 2014). Support for this idea comes from the fact that
650 more prognathic species tend to have more rugae: flat faced humans typically have 3-6 palatal
651 rugae (Hauser et al., 1989; Jayasankar et al., 2016), mice have 8-9 rugae (Peterkova et al., 1987),

652 and prognathic pigs have 20-25 rugae (Tonge and McCance, 1965). Based on 1) the expectation
653 that interspecies differences are extensions of milder intra-species differences and 2) the direct
654 early associations between palatal segments and upper jaw bone morphogenesis, we
655 hypothesized that strain-specific contributions of individual bones to upper jaw length (Percival
656 et al., 2016) would be produced by strain-specific differences in early embryonic A-P palatal
657 segment elongation.

658 We identified small, but significant strain-associated differences in facial shape and
659 palatal segment length. Embryonic facial shape differences between strains (Figs. 12 & 13; Table
660 2; Supporting Fig. 6) may represent ontogenetic shifts in the relationship of various facial
661 structures or shifts in the relative timing of normal developmental events occurring within
662 different parts of the face. Subtle differences in embryonic palatal segment proportions were
663 identified between the strains when considering the entire embryonic series at once, but these
664 differences did not match the inter-strain differences observed in adult specimens. Additionally,
665 some proportional palatal contribution differences for NOD and C57 changed between E15 and
666 P1 as well as between P1 and adult samples. A larger sample of later embryonic ages (i.e.,
667 between E15.5 and P0) would allow us to determine when the initial NOD pattern of short
668 primary and long posterior secondary palate changes to the P1 pattern of long primary and short
669 posterior secondary palate.

670 Although changes within the RGZ growth dynamics of anterior secondary palate growth
671 may be critical for major species-specific differences in prognathism, our results did not support
672 the idea that this mechanism is primarily responsible for the adult intraspecies differences in
673 upper jaw morphology between our mouse strains. This suggests that later prenatal (after E15)
674 and postnatal growth processes play a major role in determining adult upper jaw bone

675 proportions between inbred mouse strains. Broad embryonic growth patterns shared across our
676 strains indicated that elongation of the anterior secondary palate contributes most to palatal A-P
677 growth between E11 and E15, but that growth of the primary palate derived premaxilla
678 contributed most to postnatal elongation of the upper jaw.
679
680 **Concluding Statement**
681 Our multifaceted illustration of normal midfacial growth dynamics confirmed a one-to-
682 one relationship between palatal segments and upper jaw bones during the earliest stages of
683 palatal growth, suggesting that the first formed ruga represents a consistent morphological
684 boundary between anterior and posterior secondary palate bone precursors, thus approximating
685 the position of the future maxillary-palatine suture. In addition to driving rugae formation, our
686 results suggested that interactions at the RGZ simultaneously coordinate elongation of the
687 maxillary bone primordium within the anterior secondary palate, which more than doubles in
688 length prior to palatal shelf fusion. Although RGZ-driven A-P growth of the anterior secondary
689 palate likely contributes to evolutionary changes in facial upper jaw morphology, this process
690 was not responsible for the small but significant strain-specific differences in adult upper jaw
691 bone proportions measured across three inbred mouse strains. However, measured differences in
692 early palatal segment elongation provide a useful foundation for understanding the impact of
693 background genetic effects on facial morphogenesis. Our multifaceted analysis of ontogenetic
694 trends in palatal and facial elongation provides a novel contextual framework and developmental
695 perspective within which to evaluate the impact of both non-pathogenic and pathogenic genetic
696 differences on midfacial growth and differentiation.
697

Acknowledgements

We are indebted to Benedikt Hallgrímsson for the use of his laboratory for uCT and microscopy image collection. This work was supported by start-up funds to Christopher J. Percival from Stony Brook University; NIH/NIDCR R01 grant DE028753 and UCSF Chancellor Funds from Recruitment Package to Licia Selleri who supported the personnel and all the research completed in her lab for this study; and NIH/NIDCR F32 Fellowship DE026950 to Ian Welsh. The authors of this manuscript have no conflicts of interest to declare.

Data Availability Statement

µCT images, limb bud microscopy photographs, landmark coordinate data, and associated morphometric analysis R scripts are available publicly as a dataset within Dryad (https://doi.org/10.5061/dryad.ghx3ffbvb; Welsh et al., 2024).

Author Contributions

ICW contributed to study design, acquisition and interpretation of histological images, and drafting of the manuscript. MEF contributed to acquisition, analysis, and interpretation of morphometric data, and critical revision of the manuscript. DL contributed to the design of morphometric methods, acquisition of morphometric data, measurement and analysis of limb bud images, and critical revision of the manuscript. IM contributed to acquisition of µCT images, acquisition, measurement and analysis of limb bud images, and critical revision of the manuscript. KH contributed to mouse breeding, specimen collection, histological data collection, and critical revision of the manuscript. CJP contributed to study design, acquisition of µCT images, acquisition, analysis, and interpretation of morphometric data, and drafting of the manuscript.

References

Adams, D.C., Collyer, M.L., Kaliontzopoulou, A., 2020. geomorph: Software for geometric morphometric analyses. R package version 3.3.1.https://cran.r-project.org/package=geomorph

Boughner, J.C., Wat, S., Diewert, V.M., Young, N.M., Browder, L.W., Hallgrímsson, B., 2008. Short-faced mice and developmental interactions between the brain and the face. Journal of Anatomy 213, 646–662.

Bush, J.O., Jiang, R., 2012. Palatogenesis: morphogenetic and molecular mechanisms of secondary palate development. Development 139, 231–243.

Cignoni, P., Callieri, M., Corsini, M., Dellepiane, M., Ganovelli, F., Ranzuglia, G., 2008. Meshlab: an open-source mesh processing tool., in: Eurographics Italian Chapter Conference. pp. 129–136. https://doi.org/10.2312/LocalChapterEvents/ItalChap/ItalianChapConf2008/129-136

Collyer, M.L., Adams, D.C., 2018. RRPP: An R package for fitting linear models to high-dimensional data using residual randomization. Methods in Ecology and Evolution.

Economou, A.D., Ohazama, A., Porntaveetus, T., Sharpe, P.T., Kondo, S., Basson, M.A., et al., 2012. Periodic stripe formation by a Turing mechanism operating at growth zones in the mammalian palate. Nat Genet 44, 348–351. https://doi.org/10.1038/ng.1090

Enlow, D.H., Bang, S., 1965. Growth and remodeling of the human maxilla. Am J Orthod 51, 446–464. https://doi.org/10.1016/0002-9416(65)90242-3

743 Fedorov, A., Beichel, R., Kalpathy-Cramer, J., Finet, J., Fillion-Robin, J.-C., Pujol, S., et. al.,
744 2012. 3D Slicer as an image computing platform for the Quantitative Imaging Network.
745 Magnetic Resonance Imaging 30, 1323–1341. https://doi.org/10.1016/j.mri.2012.05.001
746 Fish, J.L., 2019. Evolvability of the vertebrate craniofacial skeleton. Semin Cell Dev Biol 91,
747 13–22. https://doi.org/10.1016/j.semcdb.2017.12.004
748 Geyer, S.H., Mohun, T.J., Weninger, W.J., 2009. Visualizing vertebrate embryos with episcopic
749 3D imaging techniques. ScientificWorldJournal 9, 1423–1437.
750 https://doi.org/10.1100/tsw.2009.154
751 Hall, J., Jheon, A.H., Ealba, E.L., Eames, B.F., Butcher, K.D., Mak, S.-S., et. al., 2014.
752 Evolution of a developmental mechanism: Species-specific regulation of the cell cycle
753 and the timing of events during craniofacial osteogenesis. Dev Biol 385, 380–395.
754 https://doi.org/10.1016/j.ydbio.2013.11.011
755 Hallgrímsson, B., Jamniczky, H., Young, N.M., Rolian, C., Parsons, T.E., Boughner, J.C., et. al.,
756 2009. Deciphering the Palimpsest: Studying the Relationship between Morphological
757 Integration and Phenotypic Covariation. Evolutionary Biology 36, 355–376.
758 Hammond, N.L., Dixon, M.J., 2022. Revisiting the embryogenesis of lip and palate
759 development. Oral Dis 28, 1306–1326. https://doi.org/10.1111/odi.14174
760 Hauser, G., Daponte, A., Roberts, M., 1989. Palatal rugae. Journal of Anatomy 165, 237–249.
761 Hilliard, S.A., Yu, L., Gu, S., Zhang, Z., Chen, Y.P., 2005. Regional regulation of palatal growth
762 and patterning along the anterior–posterior axis in mice. Journal of Anatomy 207, 655–
763 667. https://doi.org/10.1111/j.1469-7580.2005.00474.x
764 Jayasankar, P., Banker, A., Bhattacharya, A., Gandhi, R., Patel, N., Parikh, S., 2016. Quantitative
765 and qualitative analysis of palatal rugae patterns in Gujarati population: A retrospective,

766 cross-sectional study. J Forensic Dent Sci 8, 126. https://doi.org/10.4103/0975-
767 1475.195110
768 Kaucka, M., Petersen, J., Tesarova, M., Szarowska, B., Kastriti, M.E., Xie, M., et. al., 2018.
769 Signals from the brain and olfactory epithelium control shaping of the mammalian nasal
770 capsule cartilage. Elife 7, e34465. https://doi.org/10.7554/eLife.34465
771 Kawasaki, M., Kawasaki, K., Meguro, F., Yamada, A., Ishikawa, R., Porntaveetus, T., et. al.,
772 2018. Lrp4/Wise regulates palatal rugae development through Turing-type reaction-
773 diffusion mechanisms. PLoS One 13, e0204126.
774 https://doi.org/10.1371/journal.pone.0204126
775 Kouskoura, T., Kozlova, A., Alexiou, M., Blumer, S., Zouvelou, V., Katsaros, C., Chiquet, M.,
776 Mitsiadis, T.A., Graf, D., 2013. The Etiology of Cleft Palate Formation in BMP7-
777 Deficient Mice. PLos One 8, e59463. https://doi.org/10.1371/journal.pone.0059463
778 Kurihara, S., Enlow, D.H., Rangel, R.D., 1980. Remodeling reversals in anterior parts of the
779 human mandible and maxilla. Angle Orthod 50, 98–106. https://doi.org/10.1043/0003-
780 3219(1980)050<0098:RRIAPO>2.0.CO;2
781 Li, Q., Ding, J., 2007. Gene expression analysis reveals that formation of the mouse anterior
782 secondary palate involves recruitment of cells from the posterior side. Int. J. Dev. Biol.
783 51, 167–172.
784 Luo, W., Yi, Y., Jing, D., Zhang, S., Men, Y., Ge, W.-P., et. al., 2019. Investigation of Postnatal
785 Craniofacial Bone Development with Tissue Clearing-Based Three-Dimensional
786 Imaging. Stem Cells and Development 28, 1310–1321.
787 https://doi.org/10.1089/scd.2019.0104

788 Maga, A.M., 2016. Postnatal Development of the Craniofacial Skeleton in Male C57BL/6J Mice.
789 J Am Assoc Lab Anim Sci 55, 131–136.
790 Martinez-Maza, C., Rosas, A., Nieto-Díaz, M., 2013. Postnatal changes in the growth dynamics
791 of the human face revealed from bone modelling patterns. J Anat 223, 228–241.
792 https://doi.org/10.1111/joa.12075
793 Morris, Z.S., Abzhanov, A., 2021. Heading for higher ground: Developmental origins and
794 evolutionary diversification of the amniote face. Curr Top Dev Biol 141, 241–277.
795 https://doi.org/10.1016/bs.ctdb.2020.12.003
796 Murray, S.A., Morgan, J.L., Kane, C., Sharma, Y., Heffner, C.S., Lake, J., et. al., 2010. Mouse
797 Gestation Length Is Genetically Determined. PLoS ONE 5, e12418.
798 https://doi.org/10.1371/journal.pone.0012418
799 Musy, M., Flaherty, K., Raspopovic, J., Robert-Moreno, A., Richtsmeier, J.T., Sharpe, J., 2018.
800 A quantitative method for staging mouse embryos based on limb morphometry.
801 Development 145, 1–7.
802 Okano, J., Suzuki, S., Shiota, K., 2006. Regional heterogeneity in the developing palate:
803 morphological and molecular evidence for normal and abnormal palatogenesis.
804 Congenital Anomalies 46, 49–54. https://doi.org/10.1111/j.1741-4520.2006.00103.x
805 Palmer, A.R., Strobeck, C., 1986. Fluctuating Asymmetry: Measurement, Analysis, Patterns.
806 Annu. Rev. Ecol. Syst. 17, 391–421.
807 https://doi.org/10.1146/annurev.es.17.110186.002135
808 Pantalacci, S., Prochazka, J., Martin, A., Rothova, M., Lambert, A., Bernard, L., et. al., 2008.
809 Patterning of palatal rugae through sequential addition reveals an anterior/posterior

boundary in palatal development. BMC Developmental Biology 8, 116. https://doi.org/10.1186/1471-213X-8-116

Pauws, E., Hoshino, A., Bentley, L., Prajapati, S., Keller, C., Hammond, P., et. al., 2009. Tbx22null mice have a submucous cleft palate due to reduced palatal bone formation and also display ankyloglossia and choanal atresia phenotypes. Hum Mol Genet 18, 4171–4179. https://doi.org/10.1093/hmg/ddp368

Percival, C.J., Green, R., Marcucio, R., Hallgrímsson, B., 2014. Surface landmark quantification of embryonic mouse craniofacial morphogenesis. BMC Developmental Biology 14, 1-12. https://doi.org/10.1186/1471-213X-14-31

Percival, C.J., Liberton, D.K., Pardo-Manuel de Villena, F., Spritz, R., Marcucio, R., Hallgrímsson, B., 2016. Genetics of murine craniofacial morphology: diallel analysis of the eight founders of the Collaborative Cross. Journal of Anatomy 228, 96–112. https://doi.org/10.1111/joa.12382

Peterkova, R., Klepacek, I., Peterka, M., 1987. Prenatal development of rugae palatinae in mice: scanning electron microscopic and histologic studies. Journal of craniofacial genetics and developmental biology 7, 169–89.

R Core Team, 2021. R: A language and environment for statistical computing. R Foundation for Statistical Computing, Vienna, Austria [WWW Document]. URL https://www.R-project.org/

Sarnat, B.G., 1997. Some methods of assessing postnatal craniofaciodental growth: a retrospective of personal research. Cleft Palate Craniofac J 34, 159–172. https://doi.org/10.1597/1545-1569_1997_034_0159_smoapc_2.3.co_2

832 Schneider, R.A., 2015. Regulation of Jaw Length During Development, Disease, and Evolution.
833 Curr Top Dev Biol 115, 271–298. https://doi.org/10.1016/bs.ctdb.2015.08.002
834 Selleri, L., Rijli, F.M., 2023. Shaping faces: genetic and epigenetic control of craniofacial
835 morphogenesis. Nature Reviews Genetics 24, 610–626. https://doi.org/10.1038/s41576-
836 023-00594-w
837 Tamarin, A., 1982. The formation of the primitive choanae and the junction of the primary and
838 secondary palates in the mouse. American Journal of Anatomy 165, 319–337.
839 https://doi.org/10.1002/aja.1001650308
840 Tonge, C.H., McCance, R.A., 1965. Severe undernutrition in growing and adult animals: 15. The
841 mouth, jaws and teeth of pigs. British Journal of Nutrition 19, 361–372.
842 https://doi.org/10.1079/BJN19650034
843 Vora, S.R., Camci, E.D., Cox, T.C., 2015. Postnatal Ontogeny of the Cranial Base and
844 Craniofacial Skeleton in Male C57BL/6J Mice: A Reference Standard for Quantitative
845 Analysis. Front Physiol 6, 417. https://doi.org/10.3389/fphys.2015.00417
846 Welsh, I.C., Feiler, M.E., Lipman, D., Mormile, I., Hansen, K., Percival, C.J., 2024. Dryad
847 dataset: Palatal segment contributions to midfacial anterior-posterior growth.
848 https://doi.org/10.5061/dryad.ghx3ffbvb
849 Welsh, I.C., Hagge-Greenberg, A., O'Brien, T.P., 2007. A dosage-dependent role for Spry2 in
850 growth and patterning during palate development. Mechanisms of Development 124,
851 746–761. https://doi.org/10.1016/j.mod.2007.06.007
852 Welsh, I.C., Hart, J., Brown, J.M., Hansen, K., Rocha Marques, M., Aho, R.J., et. al., 2018. Pbx
853 loss in cranial neural crest, unlike in epithelium, results in cleft palate only and a broader
854 midface. Journal of Anatomy 233, 222–242. https://doi.org/10.1111/joa.12821

855 Welsh, I.C., O'Brien, T.P., 2009. Signaling integration in the rugae growth zone directs
856 sequential SHH signaling center formation during the rostral outgrowth of the palate.
857 Developmental Biology 336, 53–67. https://doi.org/10.1016/j.ydbio.2009.09.028
858 Wilson, R., McGuire, C., Mohun, T., DMDD Project, 2016. Deciphering the mechanisms of
859 developmental disorders: phenotype analysis of embryos from mutant mouse lines.
860 Nucleic Acids Res 44, D855-861. https://doi.org/10.1093/nar/gkv1138
861 Young, N.M., Hu, D., Lainoff, A.J., Smith, F.J., Diaz, R., Tucker, A.S., et. al., 2014. Embryonic
862 bauplans and the developmental origins of facial diversity and constraint. Development
863 141, 1059–1063. https://doi.org/10.1242/dev.099994
864 Yu, K., Ornitz, D.M., 2011. Histomorphological study of palatal shelf elevation during murine
865 secondary palate formation. Developmental Dynamics 240, 1737–1744.
866 https://doi.org/10.1002/dvdy.22670
867 Yu, L., Gu, S., Alappat, S., Song, Y., Yan, M., Zhang, X., et. al., 2005. Shox2-deficient mice
868 exhibit a rare type of incomplete clefting of the secondary palate. Development 132,
869 4397–4406. https://doi.org/10.1242/dev.02013
870 Yuan, Y., Loh, Y.-H.E., Han, X., Feng, J., Ho, T.-V., He, J., et. al., 2020. Spatiotemporal cellular
871 movement and fate decisions during first pharyngeal arch morphogenesis. Sci Adv 6,
872 eabb0119. https://doi.org/10.1126/sciadv.abb0119
873 Zelditch, M., Swiderski, D., Sheets, D.H., 2012. Geometric morphometrics for biologists: a
874 primer, 2nd ed. Elsevier Academic Press, San Diego.
875 Zhao, H., Feng, J., Ho, T.-V., Grimes, W., Urata, M., Chai, Y., 2015. The suture provides a niche
876 for mesenchymal stem cells of craniofacial bones. Nat Cell Biol 17, 386–396.
877 https://doi.org/10.1038/ncb3139

878

879 **Supporting Information**

880 Supporting Tables and Figures are found as a Supporting .pdf file in association with this

881 manuscript on the publisher's website.

882

883 **Tables**

884

885 Table 1 –Sample size of µCT imaged and morphometrically analyzed embryo specimens by strain and

886 forelimb based developmental age estimation, as estimated using eMOSS (Musy et al., 2018).

Limb-Based Developmental Age	C57	NOD	PWK
E11	8	12	4
E11.5	2	0	0
E12	7	3	6
E12.5	4	0	2
E13	9	3	6
E13.5	0	0	2
E14	26	6	6
E14.5	1	0	0
E15	9	4	0

887

888

889 Table 2 – Average proportional palatal segment lengths for postnatal specimens, presented as

890 percentages of total palatal length.

	C57			NOD			PWK
	P1 epithelial	P1 bone	Adult bone	P1 epithelial	P1 bone	Adult bone	Adult bone
Primary Palate / Premaxilla	18.4%	23.3%	32.4%	19.7%	24.4%	31.7%	30.7%
Ant. Sec. Palate / Maxilla	45.7%	47.5%	39.9%	49.5%	47.4%	41.8%	42.8%
Post. Sec. Palate / Palatine & Pterygoid	35.9%	29.2%	27.7%	30.8%	28.3%	26.5%	26.5%

891